Forschungszentrum Karlsruhe
in der Helmholtz-Gemeinschaft

Wissenschaftliche Berichte
FZKA 7265

Weight Functions and Stress Intensity Factors for Ring-shaped Cracks

T. Fett, G. Rizzi

Institut für Materialforschung

Mai 2007

FORSCHUNGSZENTRUM KARLSRUHE

in der Helmholtz-Gemeinschaft

Wissenschaftliche Berichte

FZKA 7265

Weight functions and stress intensity factors for ring-shaped cracks

T. Fett, G. Rizzi

Institut für Materialforschung

Forschungszentrum Karlsruhe GmbH, Karlsruhe

2007

Forschungszentrum Karlsruhe GmbH
Postfach 3640, 76021 Karlsruhe

Mitglied der Hermann von Helmholtz-Gemeinschaft
Deutscher Forschungszentren (HGF)

ISSN 0947-8620

urn:nbn:de:0005-072657

Weight functions and stress intensity factors for ring-shaped cracks

Abstract:
Ring-shaped cracks appear in many fracture mechanics problems of ceramic materials. In ceramics fracture is often caused by material inhomogeneities like spherical pores and inclusions. Failure of such inhomogeneities generally is modelled by failure of an annular crack extending around the inhomogeneity.

A simple procedure to compute the stress intensity factors is the application of the weight function method. If the weight function for the special crack problem is available, the stress intensity factor can be obtained by integration of the product of weight function and stress distribution caused by the inclusion in the case of the uncracked structure over the crack length.

In this report, the weight functions for a ring-shaped crack are derived and the stress intensity factors for remote tension and thermal loading are computed. These stress intensity factor solutions are then compared with K-factors available in literature.

Gewichtsfunktionen und Spannungsintensitätsfaktoren für Ringrisse

Kurzfassung:
Ringrisse treten verbreitet bei der bruchmechanischen Behandlung des Versagens keramischer Werkstoffe auf. Bei Keramiken und anderen spröden Werkstoffen geht der Bruch oft von Materialinhomogenitäten wie Einschlüssen und Poren aus. In solchen Fällen wird das Versagensverhalten unter Annahme eines Ringrisses um einen Einschluss modelliert. Der unter Belastung an diesem Riss auftretende kritische Spannungsintensitätsfaktor wird der Risszähigkeit gleichgesetzt.

Eine einfache Berechnungsmethode zur Bestimmung der Spannungsintensitätsfaktoren bei beliebig komplexen Spannungen ist die Gewichtsfunktionsmethode. Da Gewichtsfunktionen für Ringrisse in der Literatur nicht vorliegen, wurden diese bestimmt. Damit konnten die Spannungsintensitätsfaktoren für mechanische und thermische Belastungen berechnet und mit Literaturlösungen verglichen werden.

Contents

1. Introduction

Ceramic components fail due to unstable propagation of microscopic flaws in the form of pores, cracks, inclusions, or other material inhomogeneities resulting from manufacturing. Description of failure due to internal elliptical cracks or semi-elliptical surface cracks is well established. The same holds for pores.

In the case of inclusions, failure generally is modelled by the failure of an assumed annular crack extending around the inhomogeneity. Reference solutions for special loading cases are given in literature [1-6]. These solutions deviate significantly.

A simple method for the determination of stress intensity factors for any stress distribution is the weight function procedure. Unfortunately, weight functions for ring cracks are not available in literature. Therefore, it is the aim of this report to provide weight functions for the outer and the inner crack tip.

These solutions will then be compared with approximate weight functions resulting from the direct adjustment of appropriate set-ups to reference stress intensity factors from literature [4]. The weight function derived will then be tested by computing the stress intensity factors for loading by remote stresses and thermal mismatch stresses. As an example, the residual stress intensity factor of a Vickers indentation crack will be determined under the assumption that this crack is described by an annular crack, excluding the residual stress region. The results shall be compared with stress intensity factors based on the description of Vickers indentation cracks as cracks extending through the compressive residual stress region.

In section 3.3, application of the weight function technique will be extended to inhomogeneous stress distributions which are not rotationally symmetric with respect to the inclusion centre. Stress intensity factors will be estimated for the case of an inclusion with an annular crack located in the plane of a straight-through-the-thickness crack.
Section 4 will briefly deal with the problem of a pore with an annular crack.

Finally, it will be studied in Section 5 how the stresses in a real diffuse material inhomogeneity differ from the ideal case of an inclusion with a sharp transition from the inclusion to the bulk material.

2. The ring-shaped crack

2.1 Weight functions for the ring-shaped crack

A ring-shaped crack in a homogeneous infinite body of inner radius *R* and crack size *a* is shown in Fig. 2.1a. The two crack tips are denoted as (A) and (B).

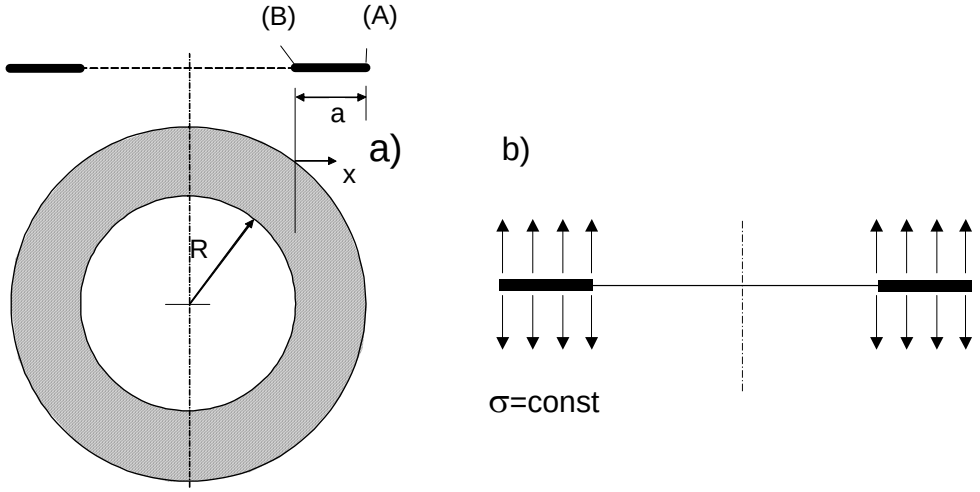

Fig. 2.1 Ring-shaped crack, a) geometry, b) reference loading case (constant stress).

Stress intensity factor solutions for the ring-shaped crack in an infinite body loaded by constant stress normal to the crack plane (Fig. 2.1b) were compiled by Rosenfelder [1].
For an arbitrarily given stress distribution $\sigma(x)$ in the uncracked body normal to the crack plane, the related stress intensity factors can be computed from

$$K_{(A)} = \int_0^a h_{(A)}\sigma(x)dx \tag{2.1}$$

$$K_{(B)} = \int_0^a h_{(B)}\sigma(x)dx \tag{2.2}$$

Unfortunately, weight functions for this special crack do not seem to be available in literature. In this report, a weight function solution for the ring-shaped crack will be derived by an interpolating procedure.
The determination of the weight function may be outlined in detail for the case of the outer crack tip (location A). In this case, several theoretical conditions have to be fulfilled:

I. The weight function for the ring-shaped crack, *h*, must be smaller than the limit weight function which is given by the case of an internal penny-shaped crack loaded only in the region where the ring extends ($x>0$), i.e. $h<h_{\lim}$ for any ratio of a/R and x/a.

II. The weight function must disappear at the inner radius *R*, $h(x=0)\rightarrow 0$.

III. At this location, the weight function must show the behaviour $h\propto\sqrt{x}$.

The upper limit solution is given as

$$h_{\lim} = \frac{2}{\sqrt{\pi(a+R)}} \frac{x+R}{\sqrt{(R+a)^2-(R+x)^2}} \tag{2.3}$$

This solution is plotted in Fig. 2.2a for several ratios of a/R.
In the case of $a/R \to 0$, the solution for the ring-shaped crack must coincide with that of the internal straight crack. Consequently, it must hold

$$h(a/R \to 0) = \sqrt{\frac{2}{\pi a}} \sqrt{\frac{x/a}{1-x/a}} \tag{2.4}$$

This solution is plotted in Fig. 2.2b together with the upper limit for $a/R=0$. The difference between these two solutions, $\Delta h(a/R \to 0)$, can be used to construct an interpolation function. If $h_{\lim,0}$ denotes the value of $h_{\lim}$ at $x/a=0$,

$$h_{\lim,0}\sqrt{a} = \frac{2}{\sqrt{\pi}\sqrt{(\frac{a}{R}+1)(\frac{a}{R}+2)}} \tag{2.5}$$

and $h_{\lim,0,0}$ is the value of $h_{\lim,0}$ for $a/R=0$

$$h_{\lim,0,0}\sqrt{a} = \sqrt{\frac{2}{\pi}} \tag{2.6}$$

the difference function $\Delta h(a/R)$ for any a/R can be approximated by

$$\Delta h(a/R) = \frac{h_{\lim,0}}{h_{\lim,0,0}} \Delta h(a/R \to 0) \tag{2.7}$$

and the approximate weight function reads

$$h(a/R) = h_{\lim}(a/R) - \Delta h(a/R) \tag{2.8}$$

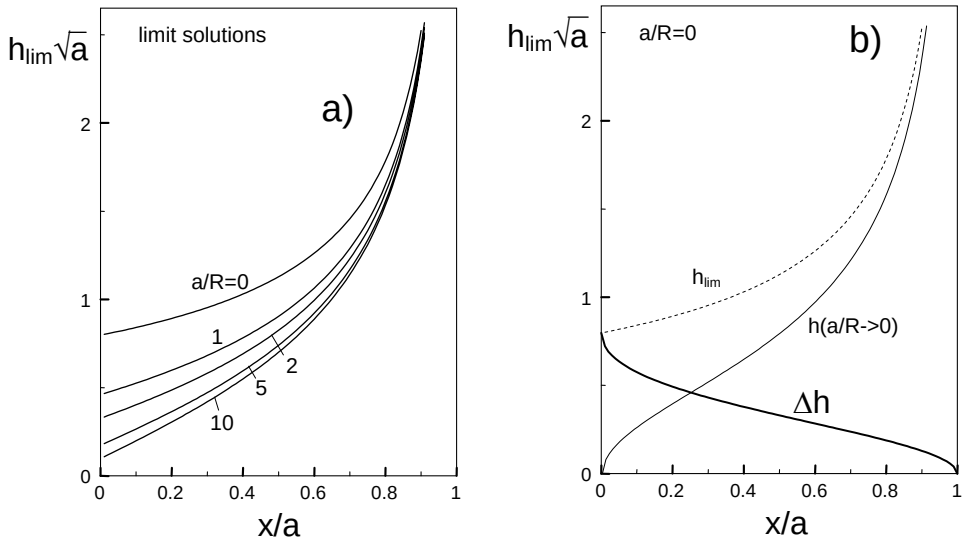

Fig. 2.2 a) Upper limit of the weight function for location (A), given by the solution for the penny-shaped crack; b) solutions for the straight crack and difference Δh between the two limit solutions for $a/R \to 0$.

In the case of the outer crack contour, the related weight function for location (B) also must fulfill the conditions (I-III). It has to be noted that this solution is not independent of that for location (A). For an arbitrarily given stress distribution over the crack (e.g. a circumferential line load), it must also fulfill the energy condition

IV. $$Q_{(B)} = Q_{(A)} \tag{2.9}$$

with $$Q_{(A)} = \int_0^a K_{(A)}^2(a')(R+a')da' \tag{2.10}$$

$$Q_{(B)} = \int_0^a K_{(A)}^2(a')(R+a-a')da' \tag{2.11}$$

The results of the numerical evaluations were fitted by

$$h_A\sqrt{a} = \frac{2}{\sqrt{\pi}\sqrt{1-\frac{x}{a}}\sqrt{\frac{a}{R}+1}}\left(\frac{1+\frac{x}{R}}{\sqrt{2+\frac{a}{R}+\frac{x}{R}}} - \frac{1-\sqrt{\frac{x}{a}}}{\sqrt{\frac{a}{R}+2}}\right) \tag{2.12}$$

$$h_B\sqrt{a} = \sqrt{\frac{2}{\pi}}\left(\sqrt{\frac{1-\frac{x}{a}}{\frac{x}{a}}} + 0.865\frac{a}{R}\exp(-C\frac{x}{a})\sqrt{\frac{x}{a}(1-\frac{x}{a})}\right), \quad C = 1+2.44\tanh(\tfrac{1}{40}\tfrac{a}{R}) \tag{2.13}$$

Figure 2.3 shows these results for variable values of *a*/*R*. It becomes obvious that the influence of the relative crack size is much stronger for location (B) than location (A).

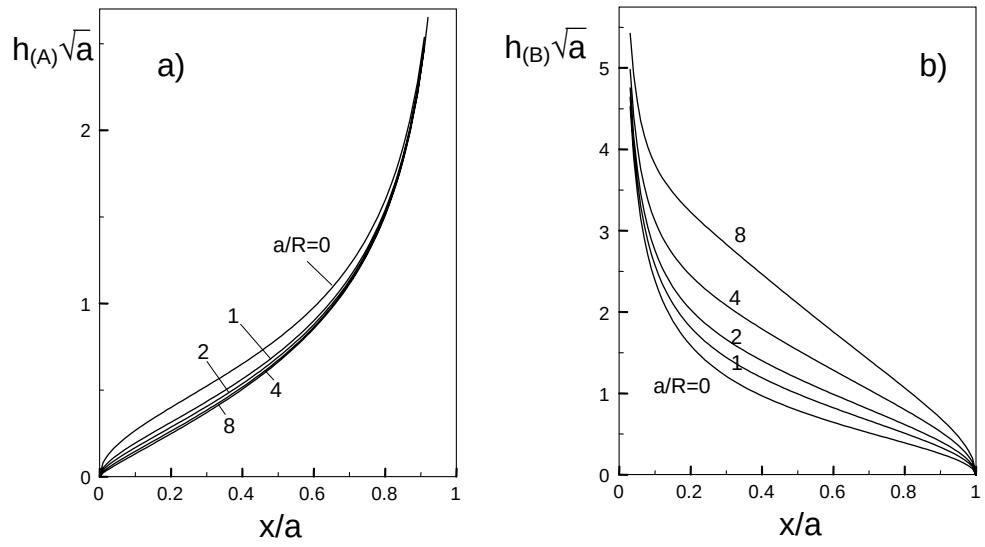

Fig. 2.3 a) Weight function for location (A), b) for location (B).

2.2 Ring crack under constant load: comparison with solutions from literature

For the reference load $\sigma=\sigma_0$=const., stress intensity factors were computed by Nied and Erdogan [2] and Tada et al. [3]. Fit relations are given by Rosenfelder [1]. The data of Nied and Erdogan [2] are expressed by

$$K_{(A)} = \sigma\sqrt{\frac{\pi a}{2}}\left[\left(1-\frac{2\sqrt{2}}{\pi}\right)\frac{1}{1+\alpha}+\frac{2\sqrt{2}}{\pi}\right] \tag{2.14}$$

$$K_{(B)} = \sigma\sqrt{\frac{\pi a}{2}}\left[\frac{1+\frac{3}{5}\alpha}{\sqrt{1+\alpha}}\right] \tag{2.15a}$$

with $\alpha=a/R$. Figure 2.4 shows these stress intensity factor solutions as curves. Data reported as curves in the 1973 edition by Tada et al. [3] were fitted by Rosenfelder as

$$K_{(A)} = \sigma\sqrt{\frac{\pi a}{2}}\left[\frac{1}{2}+\frac{\sqrt{2}}{\pi}-\left(\frac{1}{2}-\frac{\sqrt{2}}{\pi}\right)\tanh\left[\frac{5\alpha}{1+\alpha}+0.01(1+\alpha)-\frac{0.01(1+\alpha)}{\alpha}-\frac{13}{4}\right]\right] \tag{2.16}$$

$$K_{(B)} = \sigma\sqrt{\frac{\pi a}{2}}\sqrt{1+\alpha}\left[1-\frac{\alpha}{2(1+\alpha)}+\frac{9}{40}\left(\frac{|1-\alpha|}{2(1+\alpha)}\right)^{1.62} f(\alpha)\right] \tag{2.17}$$

$$f(\alpha) = \begin{cases} 0 & \text{for } \alpha < 1 \\ 1 & \text{for } \alpha > 1 \end{cases} \tag{2.18}$$

These solutions are also introduced in Fig. 2.4. The results obtained with the weight functions (2.12) and (2.13) are shown by the circles. There is an excellent agreement between the weight function results and those of Nied and Erdogan.
In the 1985 edition of Tada's handbook [3], closed-form expressions are given by

$$K_{(A)} = \sigma\sqrt{\frac{\pi a}{2}}\left(1-0.116\frac{\alpha}{1+\alpha}+0.016\left(\frac{\alpha}{1+\alpha}\right)^2\right) \tag{2.19}$$

$$K_{(B)} = \sigma\sqrt{\frac{\pi a}{2}}\,\frac{1-0.36\frac{\alpha}{1+\alpha}+0.0676\left(\frac{\alpha}{1+\alpha}\right)^2}{\sqrt{1-\frac{\alpha}{1+\alpha}}} \tag{2.20a}$$

as shown in Fig. 2.4.
A comparison of stress intensity factor relations for location (A) reveals an excellent agreement of all solutions for $a/R>2$. The agreement of solutions (2.14), (2.19), and the weight function results is excellent for any a/R.
A comparison for location (B) reveals clear deviations between the different solutions. These discrepancies were the reason for a more detailed analysis. The limit case of $K_{(B)}$ must be [3]

$$K_{(B)} \to \sigma\sqrt{\frac{\pi a}{2}}\,\frac{\sqrt{32}}{\pi^2\sqrt{1-\frac{\alpha}{1+\alpha}}} \tag{2.21}$$

This limit is not fulfilled for (2.15a) and (2.20a). The reason in (2.20a) is a typing error. The sign in front of the quadratic term must be negative, i.e.

$$K_{(B)} = \sigma\sqrt{\frac{\pi a}{2}}\,\frac{1-0.36\frac{\alpha}{1+\alpha}-0.0676\left(\frac{\alpha}{1+\alpha}\right)^2}{\sqrt{1-\frac{\alpha}{1+\alpha}}} \qquad (2.20b)$$

Equation (2.15a) can be improved by

$$K_{(B)} = \sigma\sqrt{\frac{\pi a}{2}}\left[\frac{1+\frac{\sqrt{32}}{\pi^2}\alpha+\left(\frac{3}{5}-\frac{\sqrt{32}}{\pi^2}\right)\frac{\alpha}{1+\alpha}}{\sqrt{1+\alpha}}\right] \qquad (2.15b)$$

The improved relations (2.15b) and (2.20b) are plotted in Fig. 2.5 together with the weight function results. Now, a good agreement is found also for location (B).

For location (A), use of eqs.(2.14) and (2.19) is recommended. At location (B), eqs.(2.15b) and (2.20b) seem to be the best relations.

An analytical evaluation of the weight function integrals is possible in special cases only. Under constant stress, the integration yields

$$K_{(A)} = \sigma\sqrt{\pi a}\,\frac{\pi - 4[1-\sqrt{\frac{\alpha+2}{\alpha}}\arctan\sqrt{\frac{\alpha}{\alpha+2}}]+\frac{8}{3}\alpha\,\mathrm{Hypergeometric2}F1(\frac{1}{2},2,\frac{5}{2},-\frac{\alpha}{\alpha+2})}{\pi\sqrt{(1+\alpha)(2+\alpha)}} \qquad (2.22)$$

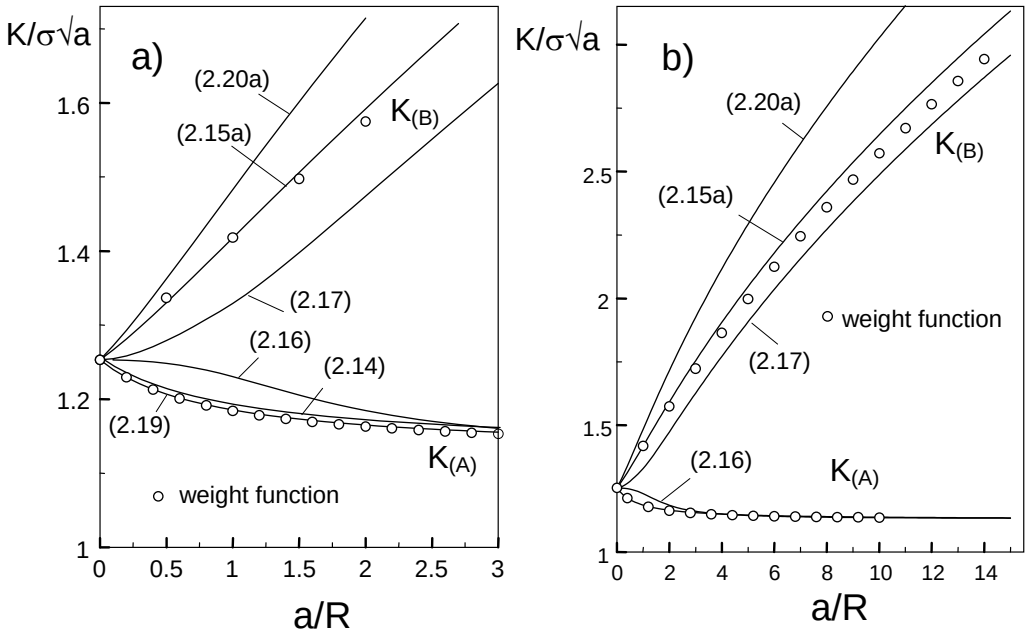

Fig. 2.4 Stress intensity factors for a ring-shaped crack under constant stress.

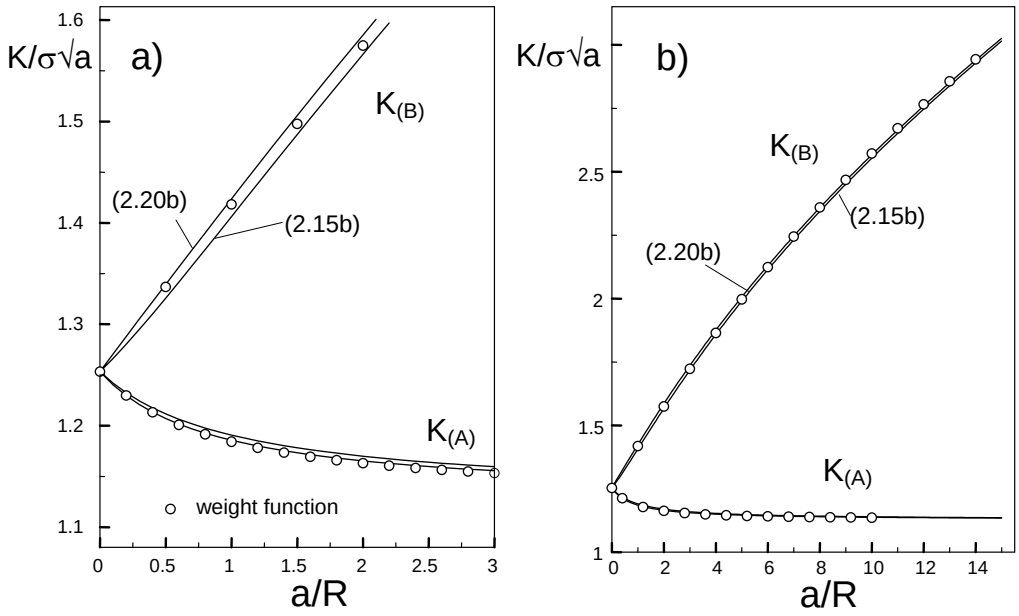

Fig. 2.5 Corrected misprints and improvements of stress intensity factor solutions for a ring-shaped crack under constant stress.

2.3 Rough weight function approximations

The weight functions derived are expected to be highly accurate. A disadvantage is the complicated structure of the relations. For evaluations with a reduced degree of approximation, simplified weight functions may be of advantage. Such weight functions can be derived easily by adjusting *h* to simple reference stress intensity factor solutions [4].
If the weight functions are approximated by

$$h_{(A)} = \sqrt{\frac{2}{\pi a}}\left(\sqrt{\frac{\frac{x}{a}}{1-\frac{x}{a}}} + D_{(A)}\sqrt{\frac{x}{a}\left(1-\frac{x}{a}\right)} \right) \tag{2.23}$$

$$h_{(B)} = \sqrt{\frac{2}{\pi a}}\left(\sqrt{\frac{1-\frac{x}{a}}{\frac{x}{a}}} + D_{(B)}\sqrt{\frac{x}{a}\left(1-\frac{x}{a}\right)} \right) \tag{2.24}$$

the stress intensity factors for σ=const. result as

$$K_{(A)} = \sigma\sqrt{\frac{a\pi}{32}}\left(D_{(A)} + 4\right) \tag{2.25}$$

$$K_{(B)} = \sigma\sqrt{\frac{a\pi}{32}}\left(D_{(B)} + 4\right) \tag{2.26}$$

Coefficients $D_{(A)}$ and $D_{(B)}$ are obtained from the solution of Tada [3]. With eqs.(2.19) and (2.20a) as the reference solutions it holds

$$D_{(A)} = -4\left(0.116\,\frac{\alpha}{1+\alpha} - 0.016\left(\frac{\alpha}{1+\alpha}\right)^2\right) \tag{2.27}$$

$$D_{(B)} = 4\left[\left(1 - 0.36\,\frac{\alpha}{1+\alpha} - 0.0676\left(\frac{\alpha}{1+\alpha}\right)^2\right)\sqrt{1+\alpha} - 1\right] \tag{2.28}$$

Application of eqs.(2.14) and (2.15b) results in

$$D_{(A)} = 4\left(\frac{\sqrt{8}}{\pi} - 1\right)\frac{\alpha}{1+\alpha} \cong -\frac{2}{5}\frac{\alpha}{1+\alpha} \tag{2.29}$$

$$\begin{aligned} D_{(B)} &= 4\left(\frac{1+\frac{8}{5}\alpha + \frac{\sqrt{32}}{\pi^2}\alpha^2}{(1+\alpha)^{3/2}} - 1\right) \\ &\cong 4\left(\frac{1-1.6\alpha+0.76\alpha^2}{(1+\alpha)^{3/2}} - 1\right) \end{aligned} \tag{2.30}$$

Figure 2.6 represents the approximate weight functions computed with (2.27) and (2.28). In Fig. 2.7, the roughly approximated weight function at location (B) is given together with the more accurate solution (2.13).

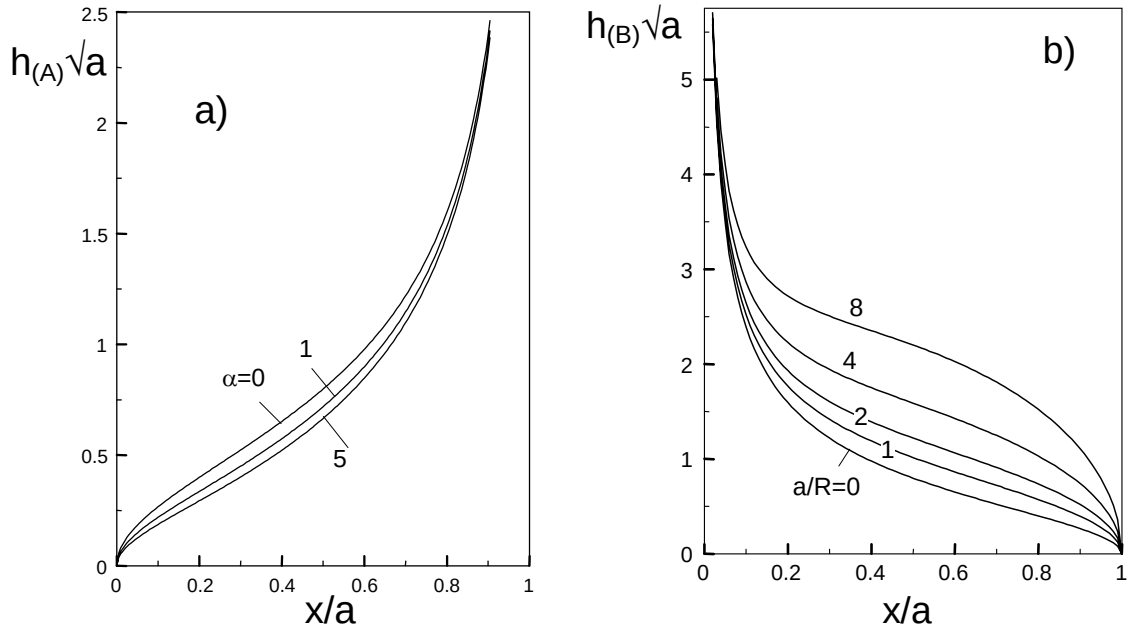

Fig. 2.6 Weight function approximations using (2.27) and (2.28) for the outer (a) and the inner (b) crack tip.

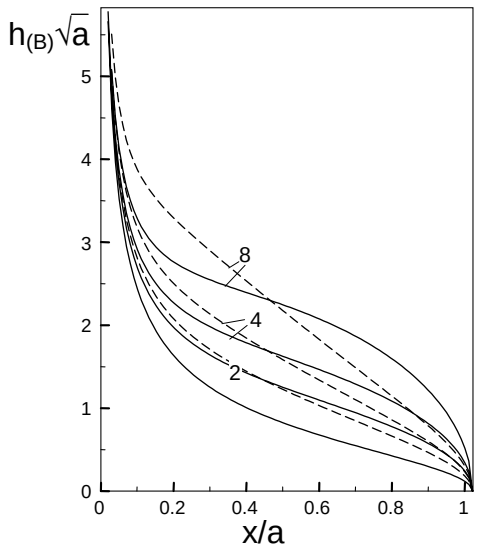

Fig. 2.7 Weight function approximation for the inner crack tip; comparison with the weight function eq.(2.13) (dashed curves).

2.4 Ring crack in an inhomogeneous non-radial symmetric stress field

2.4.1 Linear stress distribution

In section 1, the weight functions for the ring-shaped crack were derived for the case of rotational symmetry, i.e. they do not depend on the angle along the circumference. Here, it shall be checked whether the weight functions derived are also applicable to non-radial symmetric stresses. Especially for the case of $a/R \to 0$ (the so-called Griffith crack), the weight functions are applicable a priori to any type of stress distribution.

As an example, the linear stress distribution

$$\sigma = \sigma_1 \frac{\xi}{R+a} \tag{2.31}$$

may be considered with the stress value $\sigma=\sigma_1$ occurring at the outer radius (i.e. at $\xi=R+a$). The stress along the radial x-axis (see Fig. 2.8) is then given by

$$\sigma = \sigma_1 \frac{R+x}{R+a}\cos\varphi \tag{2.32}$$

Inserting the stress (2.32) into (2.1) and use of the weight function (2.12) results in the solid curve plotted in Fig. 2.9a. Use of the simplified weight function (2.23, 2.27) results in the dash-dotted curve.

The dotted line represents a solution for the linear stress distribution proposed by Tada et al. [3]. For the outer crack tip, it reads

$$K_A = \sigma_1 \sqrt{\frac{\pi a}{2}} \cos\varphi \left[1 - 0.401\frac{a}{R+a} - 0.065\left(\frac{a}{R+a}\right)^2 + 0.066\left(\frac{a}{R+a}\right)^3 \right] \tag{2.33}$$

The ratio of the weight function solution (2.12) and the literature solution (2.33) are shown in Fig. 2.9b. For $a/R<2.5$, the error of the weight function evaluation is less than 10%.

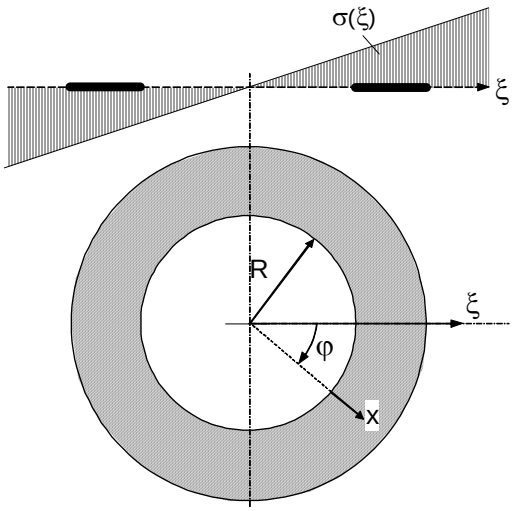

Fig. 2.8 Ring-shaped crack under a linear sress distribution.

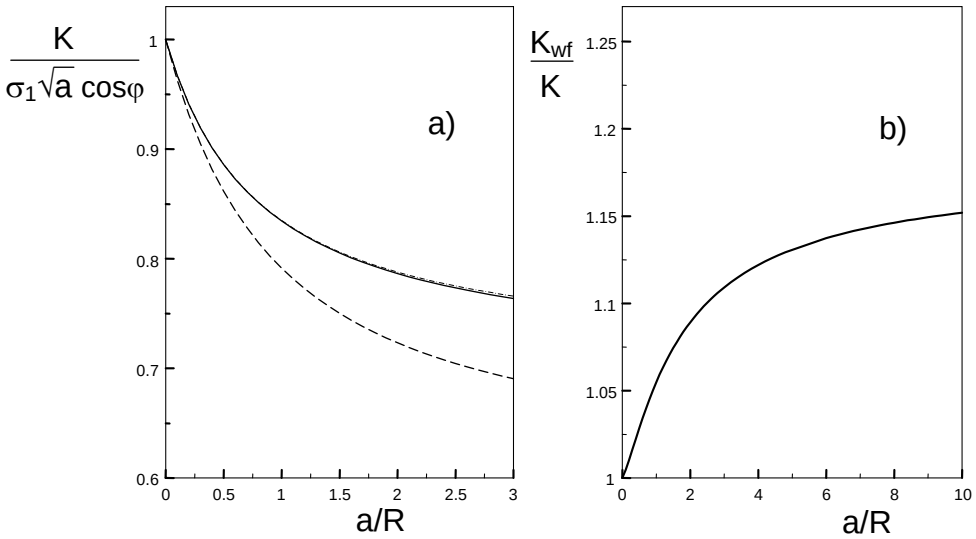

Fig. 2.9 a) Stress intensity factors for a linear stress distribution according to (2.31, 2.32), solid curve: computed with (2.12), dash-dotted curve: with (2.23, 2.27), dashed curve: solution (2.33) by Tada [3], b) ratio of the stress intensity factors of (a), K_{wf}= stress intensity factor via weight function.

In this case, the derivation of an improved weight function is also possible by adjusting h to the reference stress intensity factor solution (2.33). If the weight functions are expressed again by (2.23) and (2.24), we obtain

$$D_{(A)} = -\frac{1.604\alpha + 3.468\alpha^2 + 1.6\alpha^3}{(1+\alpha)^3} \tag{2.34}$$

$$D_{(B)} = 4\left[\frac{1}{\sqrt{1+\alpha}}\left(0.573 + \frac{0.427}{(1+\alpha)^{1/4}} - 0.26\frac{\alpha^{5/2}}{(1+\alpha)^4}\right) - 1\right] \tag{2.35}$$

2.4.1 Arbitrary stress distribution

A Taylor series expansion of the stresses along the axis ξ reads

$$\sigma(\xi) = \sigma(0) + \left.\frac{d\sigma}{d\xi}\right|_{\xi=0} \xi + \tfrac{1}{2}\left.\frac{d^2\sigma}{d\xi^2}\right|_{\xi=0} \xi^2 + \ldots \tag{2.36}$$

For the two first terms, handbook solutions exist. The constant term was addressed in detail in section 2.2. The linear term can be evaluated by using (2.33) according to Tada et al. [3]. Only the higher-order terms summarised by the remaining stress distribution $\Delta\sigma(\xi)$ of

$$\Delta\sigma(\xi) = \sigma(\xi) - \sigma_0 - \sigma_1 \frac{\xi}{a+R} \tag{2.37}$$

need to be evaluated by the non-radialsymmetric weight functions (2.23) and (2.24) with coefficients (2.34) and (2.35).

As an example of application, let us consider a ring crack located in the crack plane of a straight crack (Fig. 2.10).

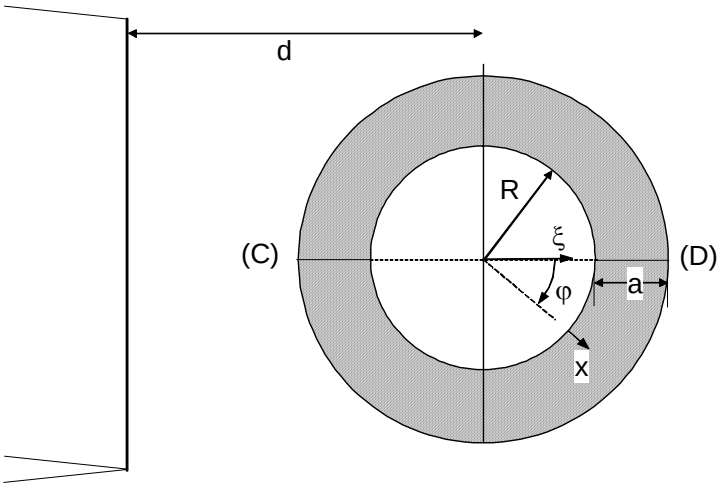

Fig. 2.10 Ring-shaped crack ahead of a straight crack.

If the ring crack is located in the prospective crack plane at a distance *d* from the tip of the straight (main) crack, the normal stress on the ring crack is given by

$$\sigma_n(\xi) = \frac{K_{appl}}{\sqrt{2\pi(d+\xi)}} \tag{2.38}$$

In (2.38), K_{appl} is the stress intensity factor of the straight crack. It is assumed here that the stress intensity factor of the main crack is not influenced significantly by the existence of the ring crack. From a Taylor series expansion with respect to ξ, the first stress terms result as

$$\sigma_0 = \frac{K_{appl}}{\sqrt{2\pi d}} \tag{2.39}$$

and

$$\sigma_1 = -\frac{K_{appl}}{\sqrt{2\pi d}} \frac{R+a}{2d} \tag{2.40}$$

The stress contribution to be evaluated with the weight function method is

$$\Delta\sigma = \frac{K_{appl}}{\sqrt{2\pi}} \left(\frac{1}{\sqrt{d+\xi}} - \frac{1}{\sqrt{d}} + \frac{\xi}{2d^{3/2}} \right), \quad \xi = (x+R)\cos\varphi \tag{2.41}$$

Now, the stress intensity factors for the ring crack may be computed for locations (C) and (D) as indicated in Fig. 2.10. The related angles are φ=0 for (D) and φ=π for (C).
In Fig. 2.11a, the total stress intensity factor K_{tot} for φ=π, including the total stress distribution $\sigma_0+\sigma_1+\Delta\sigma$ and the portion K_0+K_1 caused by the stress $\sigma_0+\sigma_1$, is plotted versus the relative distance from the main crack $d/(a+R)$. The stress intensity factors are normalised to K_0. The single stress intensity factor terms are given as

$$K_{0,(A)} = \frac{K_{appl}}{2}\sqrt{\frac{a}{d}}\left(1 - 0.116\,\tfrac{\alpha}{1+\alpha} + 0.016\left(\tfrac{\alpha}{1+\alpha}\right)^2\right) \tag{2.42}$$

$$K_{0,(B)} = \frac{K_{appl}}{2}\sqrt{\frac{a}{d}}\frac{1 - 0.36\,\tfrac{\alpha}{1+\alpha} - 0.0676\left(\tfrac{\alpha}{1+\alpha}\right)^2}{\sqrt{1-\tfrac{\alpha}{1+\alpha}}} \tag{2.43}$$

$$K_{1,(A)} = -\frac{K_{appl}}{2}\frac{R+a}{2d}\sqrt{\frac{a}{d}}\cos\varphi\left[1 - 0.401\frac{a}{R+a} - 0.065\left(\frac{a}{R+a}\right)^2 + 0.066\left(\frac{a}{R+a}\right)^3\right] \tag{2.44}$$

$$K_{1,(B)} = -\frac{K_{appl}}{2}\frac{R+a}{2d}\sqrt{\frac{a}{d}}\cos\varphi\frac{1}{\sqrt{1+\alpha}}\left[0.573 + \frac{0.427}{(1+\alpha)^{1/4}} - \frac{0.26}{(1+\alpha)^{3/2}}\left(\frac{\alpha}{1+\alpha}\right)^{5/2}\right] \tag{2.45}$$

$$K_{tot,(A),(B)} = K_{0,(A),(B)} + K_{1,(A),(B)} + \int_0^a h_{(A),(B)}\Delta\sigma\,dx \tag{2.46}$$

As shown in Fig. 2.11b for φ=π, the deviation between the approximation K_0+K_1 and the total stress intensity factor K_{tot} is less than 10% for $d/(a+R)>2$ and less than 2% for $d/(a+R)>4$. Similar plots are shown in Fig. 2.12 for φ=0.

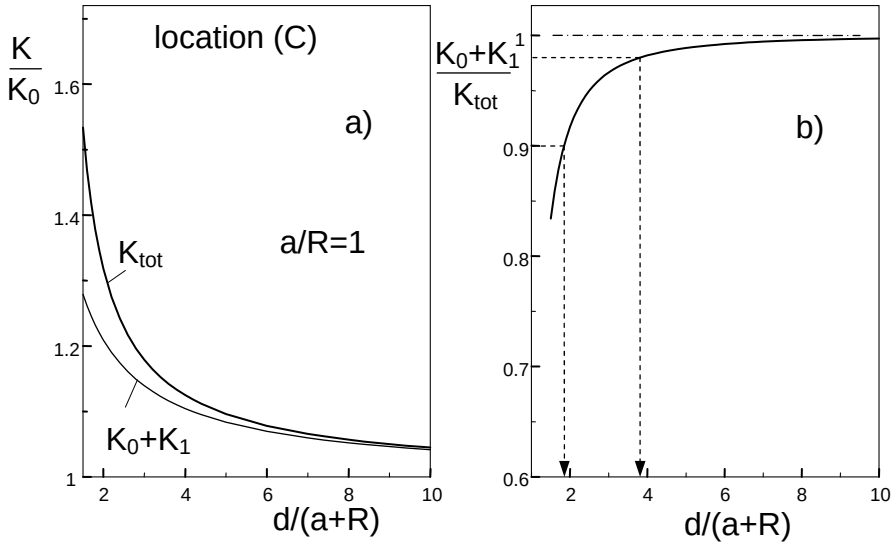

Fig. 2.11 a) Representation of the total stress intensity factor K_{tot} and the portion K_0+K_1 versus the relative distance from the main crack for φ=π, b) ratio of the two-terms approximation K_0+K_1 and the total stress intensity factor.

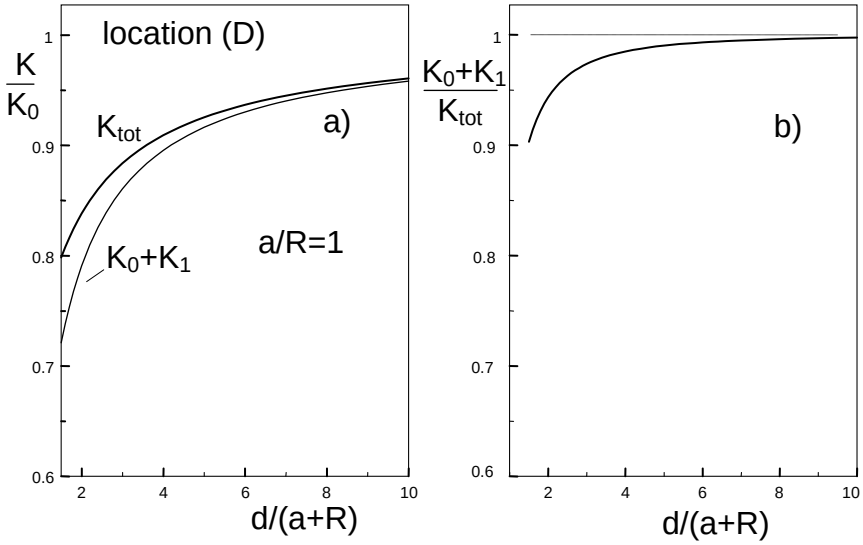

Fig. 2.12 a) Representation of the total stress intensity factor K_{tot} and the portion K_0+K_1 versus the relative distance from the main crack for φ=π, b) ratio of the two-terms approximation K_0+K_1 and the total stress intensity factor .

3. Spherical inclusion with an annular crack

Figure 3.1 shows a spherical inclusion of radius R with an annular crack of size a. The material parameters for the inclusion are E_i and ν_i and for the matrix E_m and ν_m.

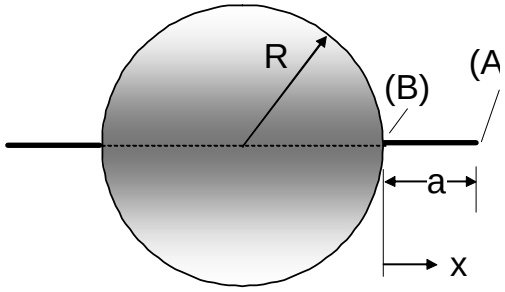

Fig. 3.1 Spherical inclusion with an annular crack.

3.1 Stress intensity factor due to thermal stresses

3.1.1 Stress intensity factor at the outer crack tip

The weight function derived in section 2 for a ring-shaped crack in a homogeneous body was used to estimate the stress intensity factor for thermal stresses at the outer crack tip (A) caused by different material properties of inclusion and matrix. At the inner crack tip (B), where the crack terminates the inclusion, a square-root shaped stress distribution does no longer appear. Hence, no stress intensity factor can be determined there. An exception is the special case of identical elastic parameters for the matrix and the inclusion. With the thermal stresses σ_n normal to the crack

$$\sigma_n = \sigma_0 \frac{R^3}{(x+R)^3} \tag{3.1}$$

and

$$\sigma_0 = \frac{(\alpha_i - \alpha_m)\Delta T}{2\bar{k}} \quad , \quad \bar{k} = \frac{1+\nu_m}{2E_m} + \frac{1-2\nu_i}{E_i} \tag{3.2}$$

the thermal stress intensity factor K^{th} at (A) obtained with the weight function (2.12) is shown in Fig. 3.2 as the thick solid curve.

The approximate weight functions according to (2.23) allow for simple analytical solutions. For the weight function coefficients given by (2.27) and (2.29), it results

$$K^{th}_{(A)} = \int_0^a h_{(A)}\sigma_n(x)\,dx = \sigma_0\sqrt{\frac{\pi a}{2}}\,\frac{1+2.134\alpha+1.284\alpha^2+0.15\alpha^3}{(1+\alpha)^{9/2}} \tag{3.3}$$

$$K^{th}_{(A)} = \int_0^a h_{(A)}\sigma_n(x)\,dx = \sigma_0\sqrt{\frac{\pi a}{2}}\,\frac{1+\frac{3}{20}\alpha}{(1+\alpha)^{5/2}} \tag{3.4}$$

In Fig. 3.2, these solutions are entered as the dashed and dash-dotted curves. Within the thickness of the curves, all these solutions coincide. In order to show the differences, Fig. 3.2c gives the relative deviations from the solution obtained with weight function eq.(2.12).

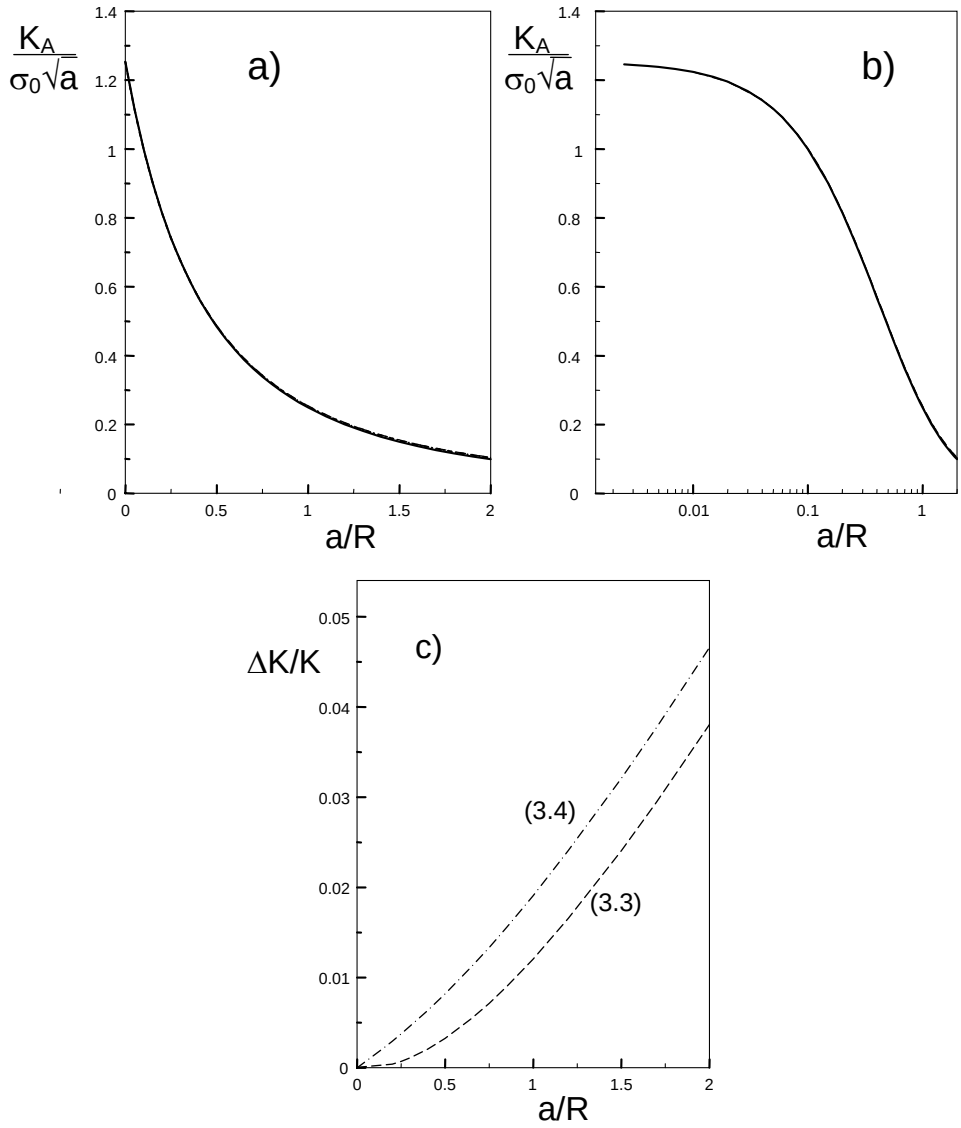

Fig. 3.2 Stress intensity factor at the outer crack tip caused by thermal stresses: (dashed: eq.(3.3), dash-dotted: eq.(3.4)).

3.1.2 Stress intensity factor at the inner crack tip

In the special case of identical elastic constants E and ν for the inclusion and the matrix, a stress intensity factor also occurs at the inner crack tip. The solution computed with the weight function (2.13) is plotted in Fig. 3.3 as the solid curve.

The approximate weight function (2.28) gives the stress intensity factor relation for this location

$$K_{(B)}^{th} = \sigma_0 \sqrt{\frac{\pi a}{2}} \frac{1 + 2.64\alpha + 2.2124\alpha^2 + 0.5723\alpha^3 + 0.75\alpha(1+\alpha)^{5/2}}{(1+\alpha)^4} \tag{3.5}$$

In Fig. 3.2, it is shown as the dashed curve. Weight function (2.30) results in

$$K_{(B)}^{th} = \sigma_0 \sqrt{\frac{\pi a}{2}} \frac{1+1.6\alpha+0.76\alpha^2+0.75\alpha(1+\alpha)^{3/2}}{(1+\alpha)^3} \tag{3.6}$$

as shown in Fig. 3.2 by the dash-dotted curve.

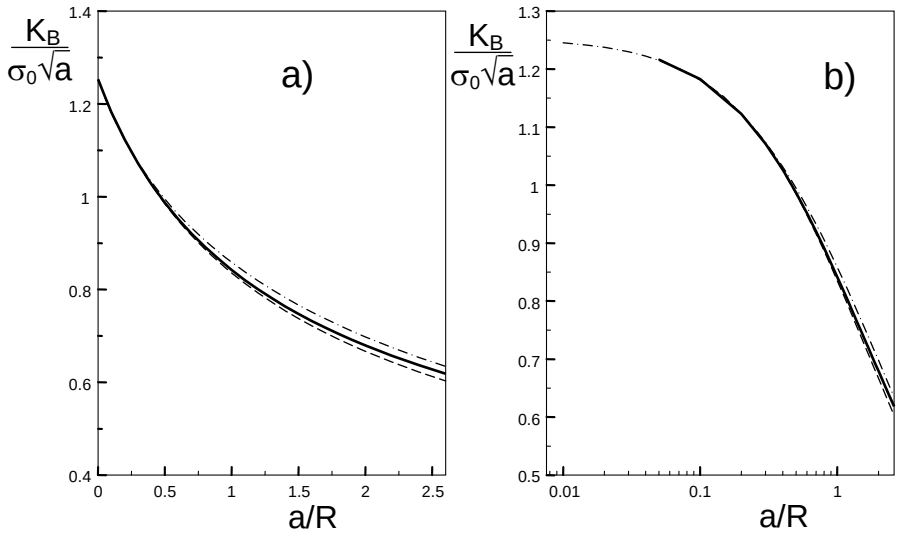

Fig. 3.3 Stress intensity factor at the inner crack tip for the case of the same elastic constants in the inclusion and matrix (dashed: eq.(3.5), dash-dotted: eq.(3.6)).

3.1.3 Comparison with stress intensity factor solutions from literature

Stress intensity factor results from literature were compiled by Rosenfelder [1]. A simple estimation procedure was proposed by Baratta [5]. This estimation is identical with the solution for constant crack-face loading by the stress at location $x=a$, i.e.

$$\sigma_n = \frac{\sigma_0}{(1+\alpha)^3} \tag{3.1a}$$

resulting in

$$K_{(A)}^{th} = \sigma_0 \sqrt{\frac{\pi a}{2}} \frac{1}{(1+\alpha)^3} \left((1-\frac{\sqrt{8}}{\pi}) \frac{1}{1+\alpha} + \frac{\sqrt{8}}{\pi} \right) \tag{3.7}$$

Since the thermal stress value at $x=a$ is the lowest one that appears on the crack face, this solution underestimates the true stress intensity factor (Fig. 3.4).

A solution from Ito [6] resulting from finite element computations reads for identical elastic properties of matrix and inclusion

$$K_{(A)}^{th} = \sigma_0 \sqrt{a}\, 0.89 \sqrt{\frac{2+\alpha}{(1+\alpha)^5(1+\nu)}} \tag{3.8}$$

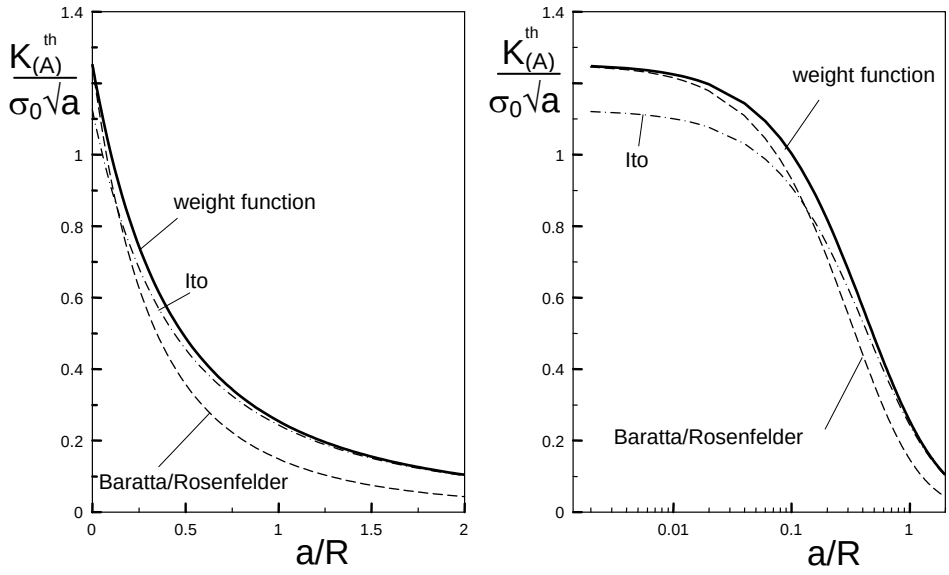

Fig. 3.4 Stress intensity factor for the inclusion with an annular crack for thermal stresses.

Whereas stress intensity factors for remote stresses increase continuously with increasing crack size, stress intensity factors under thermal stresses exhibit a maximum stress intensity factor at a/R=0.28, as can be seen from the representation in Fig. 3.5.

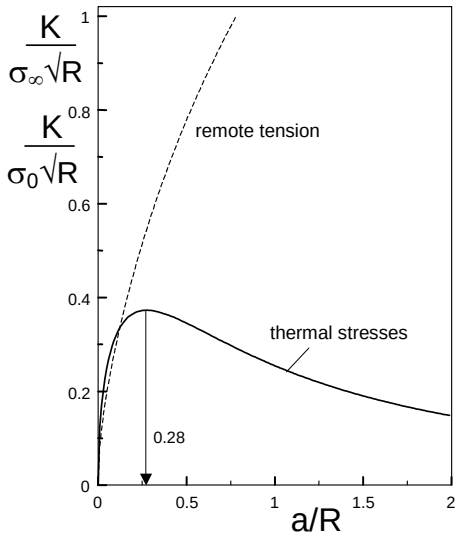

Fig. 3.5 Comparison of stress intensity factors for loading by remote tension (dashed curve) and thermal stresses.

3.1.4 Vickers indentation crack modelled as a ring crack around an expanding sphere

Below the contact area of a Vickers indenter pressed into the surface of a brittle material, a residual stress zone remains after unloading. In order to determine the stress intensity factor or the crack opening behaviour of Vickers indentation cracks under the residual stresses, a description of the expanding cavity is commonly used.

For the pressure distribution, it was proposed by Hill [7] that

$$\sigma_{res}(r) = \begin{cases} -k\sigma_0 & for \quad r < c_1 \\ \sigma_0\left((k+1)\dfrac{r-c_1}{c_2-c_1} - 1\right) & for \quad c_1 < r < c_2 \\ \sigma_0 (c_2 / r)^3 & for \quad c_2 < r \end{cases} \tag{3.9}$$

Computations of crack opening displacement were performed in [8, 9]. In this study, the crack was modelled by a half penny-shaped surface crack. The special case of (3.9)

$$c_1 = c_2 = b \tag{3.10}$$

i.e.

$$\sigma_{res}(r) = \begin{cases} -p & r < b \\ \frac{1}{2}\, p(b/r)^3 & r > b \end{cases} \tag{3.11}$$

(-*p* is the maximum pressure in the centre) was considered in detail (see Fig. 3.6a). After the indentation test, a crack opening behaviour is visible, as illustrated schematically in Fig. 3.6b. The inner radius of the open crack, *R*, can be measured from the COD profile observable on the specimen surface.

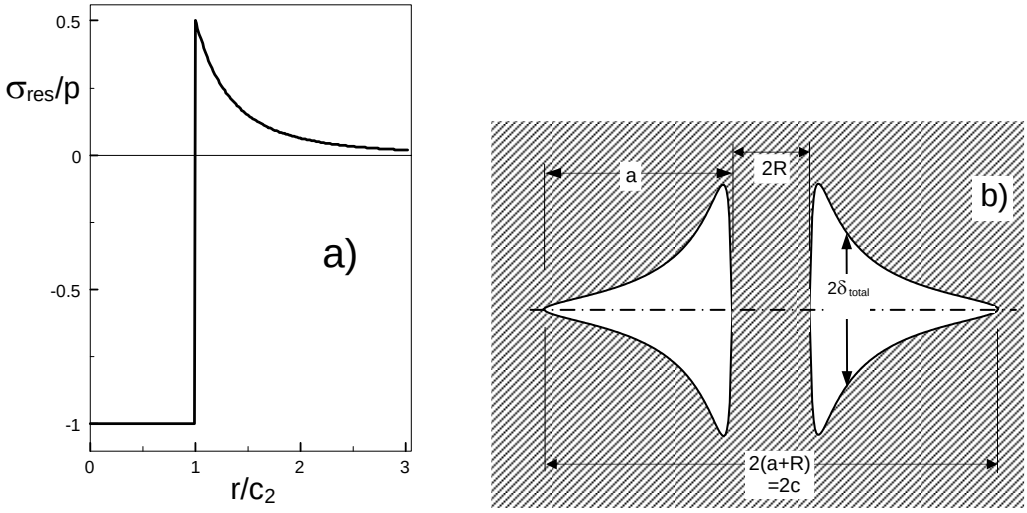

Fig. 3.6 a) Residual stresses in the uncracked body for the limit case c_1=c_2=b, b) crack opening profile on the specimen surface (schematic representation).

As a second possibility of describing the Vickers crack problem, let us model this crack here as a ring-shaped crack around the central compressive zone. The inner radius of the ring-shaped crack, *R*, is not necessarily identical with the size *b* of the compressive zone.
If a material without an R-curve behaviour and subcritical crack growth is considered, the inner and outer ring crack radii must result from the condition

$$K_{(A)} = K_{(B)} = K_{Ic} \tag{3.12}$$

where K_{Ic} is fracture toughness.

The stress intensity factors $K_{(A)}$ and $K_{(B)}$ were computed by inserting the stress distribution (3.11) into (2.1) and (2.2) and using the weight functions according to (2.12) and (2.13). The stress intensity factor computations have to be carried out iteratively for any fixed ratio of a/R by varying R/b until the condition (3.12) is satisfied. The total stress intensity factor at point (A) is plotted in Fig. 3.7a versus the parameter c defined as

$$c = a + R \tag{3.13}$$

The results for the ring-shaped crack are represented by the solid symbols. The open symbols are results obtained in [8, 9] under the assumption of the crack being a semi-circular one, the centre region of which is also loaded by the compressive stresses of (3.11). There is an excellent agreement of the stress intensity factors resulting for these strongly different crack assumptions. For $c/b \geq 2.5$, the fitting line reads

$$K = 0.385\, p\sqrt{b}\left(\frac{b}{c}\right)^{3/2} \tag{3.14}$$

The larger a crack is, the more does the inner crack radius "grow" into the compressive zone. This is shown in Fig. 3.7b.

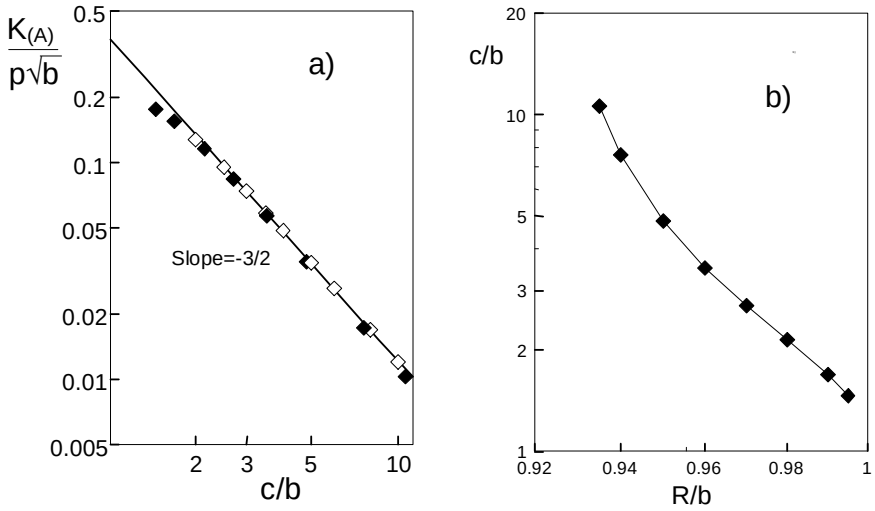

Fig. 3.7 Stress intensity factor, a) comparison of results based on the assumption of a penny-shaped crack (open symbols) with results for a ring crack (full symbols), b) change of the inner radius of the ring crack.

3.2 Stress intensity factor for remote tension

Under a remote tensile stress σ_∞, the tangential stresses at the equator of the sphere (normal to the prospective crack plane) are in the matrix

$$\sigma_n = \sigma_\infty \left[1 - \frac{A}{(1 + x/R)^3} + \frac{9B}{(1 + x/R)^5} \right] \tag{3.15}$$

with the material parameters [10]

$$A = -\frac{1}{2} + \frac{E_i + E_m - 2E_m\nu_i}{E_i + 2E_m - 4E_m\nu_i + E_i\nu_m} - \frac{1}{2}\frac{E_m(1+\nu_i)(4-5\nu_m) + E_i(1+\nu_m)}{E_m(1+\nu_i)(7-5\nu_m) + 2E_i(4-\nu_m-5\nu_m^2)} \tag{3.16}$$

$$B = \frac{E_m(1+\nu_i) - E_i(1+\nu_m)}{2E_m(1+\nu_i)(7-5\nu_m) + 4E_i(4-\nu_m-5\nu_m^2)} \tag{3.17}$$

The subscript "i" stands for inclusion and "m" for matrix. Using the approximate weight function with (2.29), integration according to (2.1) gives the solution

$$K_\infty = \sigma_\infty\sqrt{\frac{\pi a}{2}}\left(\frac{1+\frac{9}{10}\alpha}{1+\alpha} - \frac{1+\frac{3}{20}\alpha}{(1+\alpha)^{5/2}}A + 9\frac{1+\frac{13}{20}\alpha+\frac{11}{40}\alpha^2+\frac{3}{64}\alpha^3}{(1+\alpha)^{9/2}}B\right) \tag{3.18}$$

In Fig. 3.8, the numerical solution of (2.12) represented as the solid curve is compared with the approximation (3.18) shown by the dashed curve and the rough approximation derived by Baratta [5]

$$K_\infty = \sigma_\infty\sqrt{\frac{\pi a}{2}}\left(1 - \frac{A}{(1+\alpha)^3} + \frac{9B}{(1+\alpha)^5}\right)\left[\left(1-\frac{\sqrt{8}}{\pi}\right)\frac{1}{1+\alpha} + \frac{\sqrt{8}}{\pi}\right] \tag{3.19}$$

and displayed by the dash-dotted curve. Whereas deviations between (3.18) and the numerical solution are hardly visible, the estimation of Baratta deviates significantly.

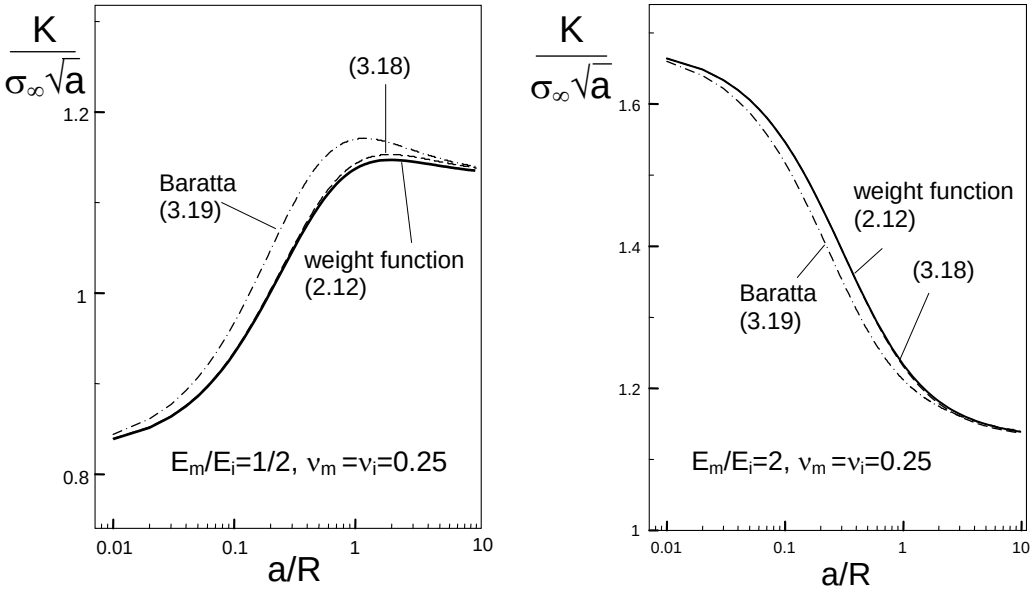

Fig. 3.8 Stress intensity factors for a spherical inclusion with an annular crack, comparison of the numerical solution obtained with the weight function (2.12) and the closed-form expressions eqs.(3.18) and (3.19).

3.3 Inclusion with an annular crack under a varying applied stress

The stress intensity factor computations for inclusions with an annular crack have been carried out so far for axis-symmetric stress distributions. For the case of stresses varying over the cross-section as illustrated by Fig. 3.9, an estimation procedure is proposed.

The stresses may be expressed again by eq.(2.36)

$$\sigma(\xi) = \sigma(0) + \left.\frac{d\sigma}{d\xi}\right|_{\xi=0} \xi + \tfrac{1}{2}\left.\frac{d^2\sigma}{d\xi^2}\right|_{\xi=0} \xi^2 + \ldots \tag{2.36}$$

The stress intensity factor solution under this stress is approximated by the superposition of the solution K_∞ for a constant remote tensile stress $\sigma_\infty=\sigma(0)$, eq.(3.18) or (3.19), with the stress intensity factor K_{ring} representing the solution for the ring-crack under the varying stresses as given by eqs.(2.42-2.46). In this approximation the total stress intensity factor at the outer crack tip (A) is given by

$$K_{(A)} \cong K_\infty(\sigma_\infty = \sigma(0)) + K_{(A),ring} \tag{3.20}$$

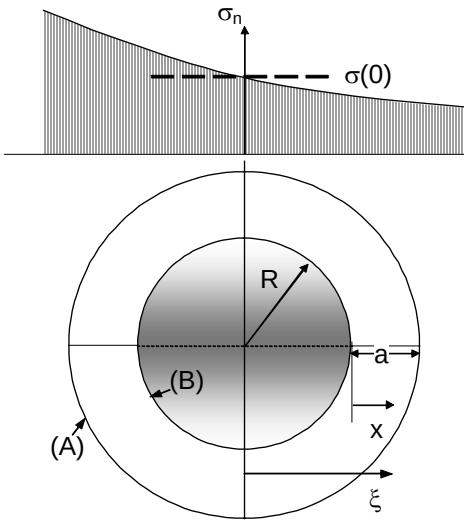

Fig. 3.9 Inclusion with an annular crack for non-axissymmetric stress distributions.

Special case: inclusion with an annular crack in front of a through-the-thickness crack

If the spherical inclusion is located in the plane of a straight-through crack (Fig. 3.10), the constant stress term $\sigma(0)$ is given by

$$\sigma(0) = \frac{K_{appl}}{\sqrt{2\pi d}} \tag{3.21}$$

and the stress intensity factor can be computed from eq.(3.20). For inclusions not too close to the main crack, the stress intensity factors for the annular crack are approximated by

$$K_{(A),ring} = K_{0,(A)} + K_{1,(A)} + \int_0^a h_{(A)} \Delta\sigma \, dx \cong K_{0,(A)} + K_{1,(A)} \tag{3.22}$$

with an error of less than 10% for $d/(a+R)>2$ and less than 2% for $d/(a+R)>4$, as concluded in section 2.4.1.
Finally, we obtain

$$K_{(A)} \cong K_{\infty}(\sigma_{\infty} = \sigma(0)) + K_{0,(A)} + K_{1,(A)} \tag{3.23}$$

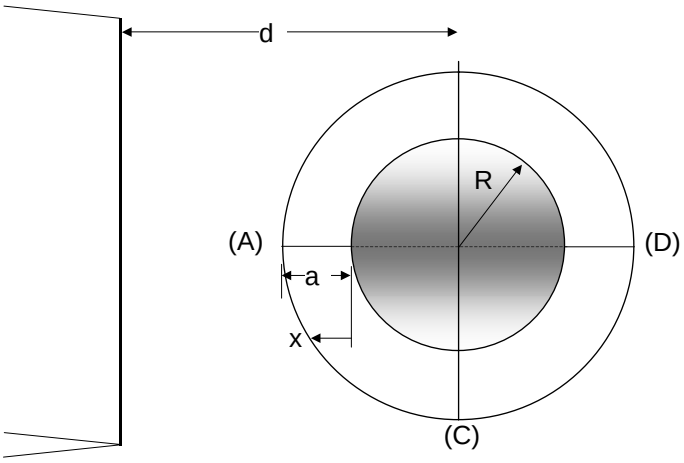

Fig. 3.10 Spherical inclusion with an annular crack ahead of a straight crack.

4. Pore with an annular crack

The stresses of a pore under remote tensile loading can be obtained from the solution of a spherical inclusion by setting E_i=0. However, this is impossible for the stress intensity factors, since the crack is no longer closed at the sphere surface and, consequently, the weight function for an annular crack is no longer valid. In this case, the weight function is given in [4]. It reads

$$h = \frac{1}{(1+2\alpha)^2} h_1 + \left(1 - \frac{1}{(1+2\alpha)^2}\right) h_2 \tag{4.1}$$

with

$$h_1 = \sqrt{\frac{2}{\pi a}} \left(\frac{1}{\sqrt{1-\frac{x}{a}}} + 0.498(1-\tfrac{x}{a})^{1/2} + 0.5416(1-\tfrac{x}{a})^{3/2} - 0.1928(1-\tfrac{x}{a})^{5/2} \right) \tag{4.2}$$

and

$$h_2 = \frac{2}{\sqrt{\pi(a+R)}} \frac{x+R}{\sqrt{(a+R)^2 - (x+R)^2}} \tag{4.3}$$

Under remote tension σ_∞, the stresses normal to the prospective crack are

$$\sigma_n = \sigma_\infty \left[1 + \frac{1}{2(7-5\nu)} \left(\frac{4-5\nu}{(1+x/R)^3} + \frac{9}{(1+x/R)^5} \right) \right] \tag{4.4}$$

Several solutions for the stress intensity factor are known. A solution of the stress intensity factor was given by Baratta [11,12]

$$\frac{K}{\sigma_\infty \sqrt{\pi a}} = (1.12 - 0.3\arctan(\alpha)) \left(\frac{4-5\nu}{2(7-5\nu)(1+\alpha)^3} + \frac{9}{2(7-5\nu)(1+\alpha)^5} + 1 \right) \tag{4.5}$$

In [4], it is proposed that

$$\frac{K}{\sigma_\infty \sqrt{\pi a}} = \frac{2}{\pi} \sqrt{\frac{\alpha+2}{\alpha+1}} \left[\frac{1}{2(1+\alpha)^2} + \frac{3}{(7-5\nu)(1+\alpha)^4} + 1 \right] + \tfrac{1}{3} \frac{9-5\nu}{(7-5\nu)(1+2\alpha)^2} \tag{4.6}$$

Green [13,14] derived

$$\frac{K}{\sigma_\infty \sqrt{\pi a}} = \frac{2}{\pi} \sqrt{\frac{\alpha+2}{\alpha+1}} \left[\frac{4-5\nu}{2(7-5\nu)(1+\alpha)^2} + \frac{3(2+(1+\alpha)^2)}{2(7-5\nu)(1+\alpha)^4} + 1 \right] + \frac{1}{\pi} \sqrt{\frac{\alpha+2}{(\alpha+1)^5}} \tag{4.7}$$

These solutions are plotted in Fig. 4.2.

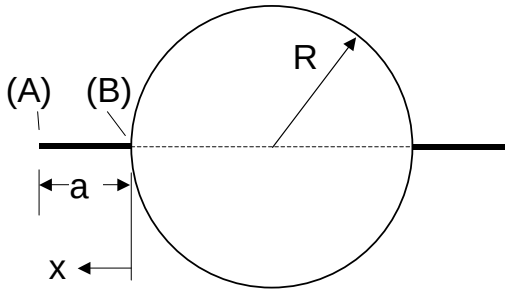

Fig. 4.1 Spherical pore with an annular crack.

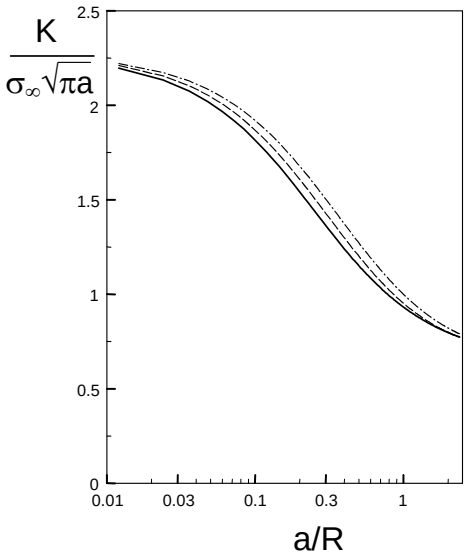

Fig. 4.2 Stress intensity factor for a pore with an annular crack under remote tension for ν=0.25 (solid: [11,12], dashed: [4], dash-dotted: [13,14]).

5. Stresses at spherical inhomogeneities

5.1 Inhomogeneity with smooth transition of thermal expansion coefficient

In the examples covered by section 3, inclusions with an abruptly changing thermal expansion coefficient α at the location x=0 were considered. In real cases, the variation of the material properties may change continuously as, for instance, in case of diffusion layers at the sphere surface. Below, the *principal effect* of continuously varying material properties on the height of thermal stresses will be shown.

Figure 5.1 shows a spherical inclusion with radius R, surrounded by a transition region in which α changes from the inclusion value α_i to the matrix value α_m. For reasons of simplicity, it is assumed that only the thermal expansion coefficient α may vary. Young's modulus and Poisson's ratio are assumed to be constant in all regions. This rough simplification allows to derive analytical expressions for the stresses.

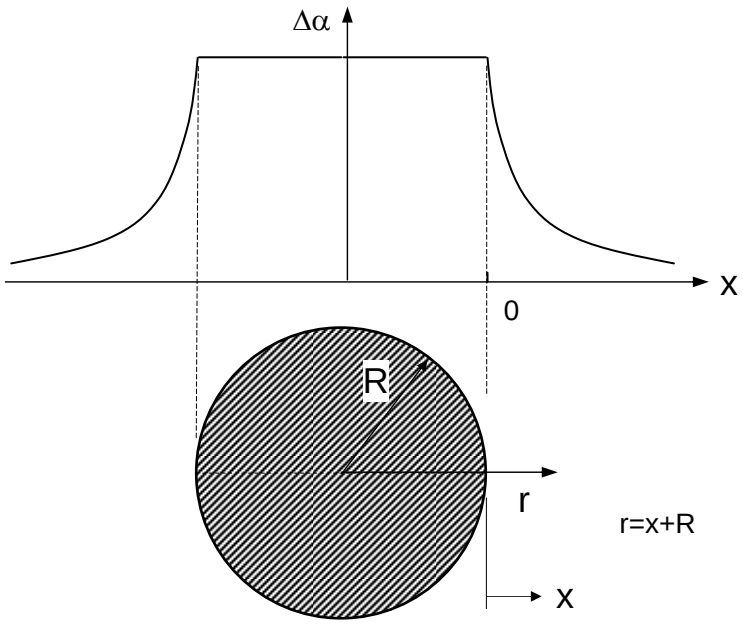

Fig. 5.1 Spherical inclusion with a smooth transition of the thermal expansion coefficient α.

For instance, a simple assumption for $\Delta\alpha$ is

$$\Delta\alpha = \begin{cases} a_i - a_m & for \;\; x < 0 \\ (\alpha_i - \alpha_m)\exp(-\eta\, x / R) & for \;\; x > 0 \end{cases} \tag{5.1}$$

Timoshenko and Goodier [15] (section 152) computed the stresses for a sphere with a constant thermal expansion coefficient α and variable temperature T. For thermal expansion as the reason of stresses, the product $\Delta\alpha\Delta T$ is responsible. This allows to rewrite the equations for the radial σ_r and tangential stress σ_t in [15] as

$$\sigma_t = \frac{E\Delta T}{1-\nu}\left(\frac{1}{r^3}\int_0^r \Delta\alpha\, r^2 dr - \Delta\alpha\right) \tag{5.2}$$

$$\sigma_r = -\frac{2E\Delta T}{1-\nu}\frac{1}{r^3}\int_0^r \Delta\alpha\, r^2 dr \quad , r = x + R \tag{5.3}$$

With the abbreviation ρ=*r*/*R* and the normalisation

$$\sigma' = \frac{1-\nu}{E\Delta T(\alpha_i - \alpha_m)}\,\sigma \tag{5.4}$$

the tangential stress results as

$$\sigma'_t = \tfrac{1}{3}\begin{cases} -2 & r < R \\ \dfrac{1}{\eta^3\rho^3}[6+6\eta+3\eta^2+\eta^3-3(1+\eta\rho)(2+\eta^2\rho^2)\exp(-\eta(\rho-1))] & r > R \end{cases} \tag{5.5}$$

and the radial component as

$$\sigma'_r = -\tfrac{2}{3}\begin{cases} 1 & r < R \\ \dfrac{1}{\eta^3\rho^3}[6+6\eta+3\eta^2+\eta^3-3(2+2\eta\rho+\eta^2\rho^2)\exp(-\eta(\rho-1))] & r > R \end{cases} \tag{5.6}$$

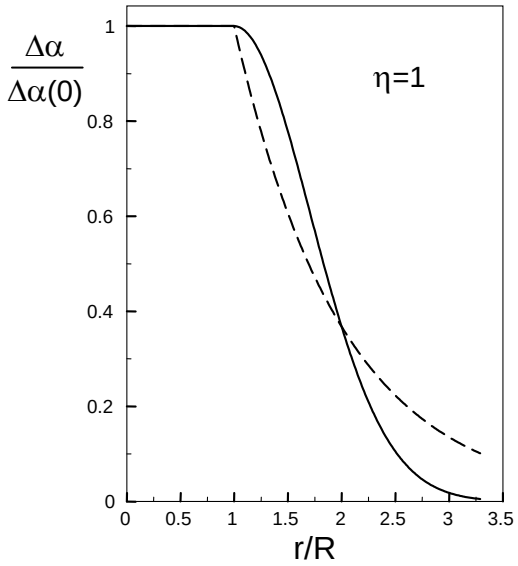

Fig. 5.2 Normalised difference in thermal expansion coefficients according to eq.(5.1) (dashed curve) and eq.(5.7) (solid curve).

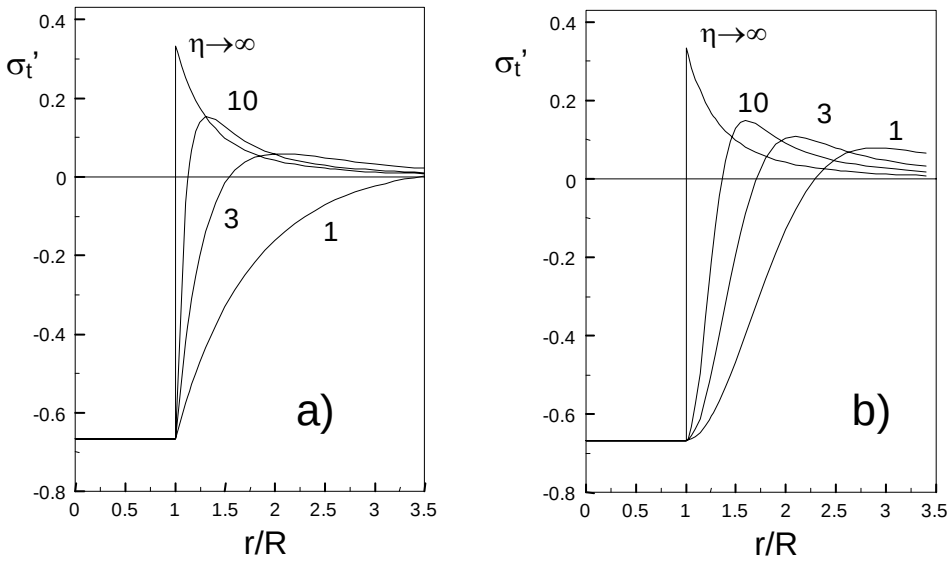

Fig. 5.3 Normalised tangential stresses for several values of η, a) eq.(5.5) and b) eq.(5.8).

A second possibility to model a smooth change in α is, for example,

$$\Delta\alpha = \begin{cases} a_i - a_m & for\ \ x < 0 \\ (\alpha_i - \alpha_m)\exp(-\eta\, x^2 / R^2) & for\ \ x > 0 \end{cases} \tag{5.7}$$

The tangential stresses result as

$$\sigma'_t = \begin{cases} -\dfrac{2}{3} & for\ \ r < R \\ \dfrac{1}{12\rho^3}\left(\dfrac{4(3+\eta) - 6(1+\rho+2\eta\rho^3)\exp(-\eta(\rho-1)^2)}{\eta} + \right. & \\ \left. + \dfrac{3(1+2\eta)\sqrt{\pi}\,\mathrm{erf}[\sqrt{\eta}(\rho-1)]}{\eta^{3/2}} \right) & for\ \ r > R \end{cases} \tag{5.8}$$

and the radial component as

$$\sigma'_r = -2\begin{cases} \dfrac{1}{3} & for\ \ r < R \\ \dfrac{1}{12\rho^3}\left(\dfrac{4(3+\eta) - 6(1+\rho)\exp(-\eta(\rho-1)^2)}{\eta} + \right. & \\ \left. + \dfrac{3(1+2\eta)\sqrt{\pi}\,\mathrm{erf}[\sqrt{\eta}(\rho-1)]}{\eta^{3/2}} \right) & for\ \ r > R \end{cases} \tag{5.9}$$

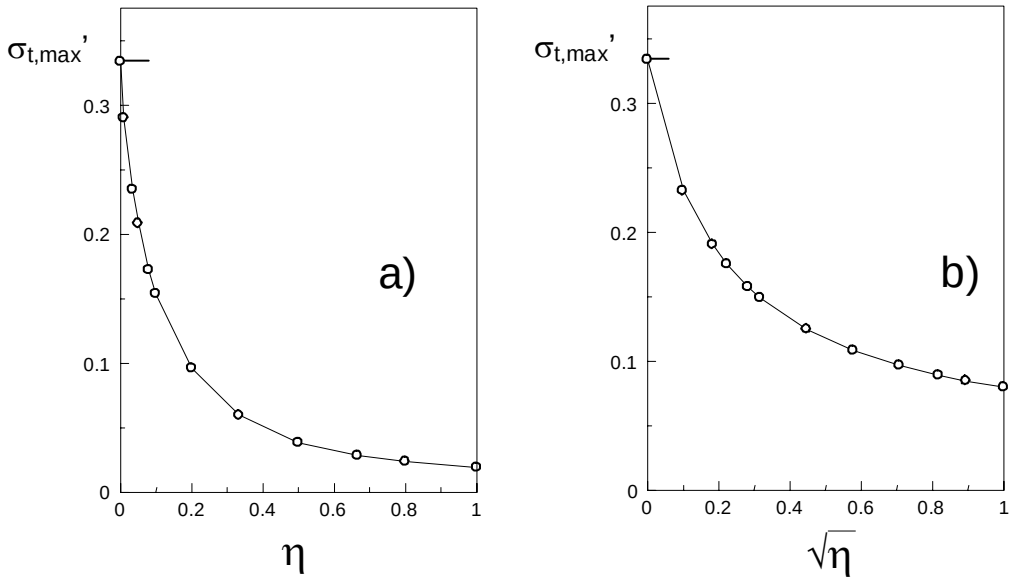

Fig. 5.4 Normalised maximum tangential stresses versus η, a) eq.(5.5) and b) eq.(5.8).

Figure 5.2 shows the $\Delta\alpha$ variations according to (5.1) and (5.7) in a normalised representation. In Fig. 5.3, the tangential stresses are plotted for the two $\Delta\alpha$ distributions. It becomes clear from these plots that the maximum tensile stresses decrease significantly with decreasing η, i.e. for increasing transition zones. The same tendency must occur for the stress intensity factors of annular cracks located in these reduced stress fields. Figure 5.4 represents the maximum tensile stresses as a function of η. The radial stresses are shown in Fig. 5.5 for $\eta=1$ and $\eta\rightarrow\infty$.

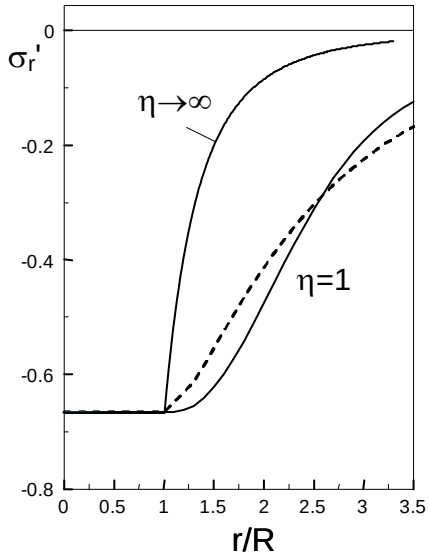

Fig. 5.5 Normalised radial stresses for $\eta=1$, dashed curve: eq.(5.1), solid curve: eq.(5.7); inclusion with sharp contour: $\eta\rightarrow\infty$.

5.2 Diffuse inhomogeneities with identical Young's modulus

5.2.1 Gaussian distribution of thermal expansion mismatch

In some cases, an inclusion or a pore may not be described sufficiently by a sphere with a sharp radius having sectionally constant material parameters. For instance, local agglomerations or density fluctuations in a material will result in more "diffuse inhomogeneities". This will also be true for very small inclusions in a material with radii comparable to the microstructure (e.g. glass regions of higher density in a matrix of mean density).
For the distribution of the thermal expansion coefficient in such an inhomogeneity, a simple dependency is chosen

$$\Delta\alpha = \Delta\alpha(0)\exp[-(r/R)^2] \tag{5.10}$$

in which the sphere radius is defined as the distance, at which the mismatch $\Delta\alpha$ is 1/e (i.e. 36.7%) of the maximum value in the centre. This dependency is plotted in Fig. 5.6a.

The thermal stresses under the assumption of constant elastic parameters are then obtained from (5.2) and (5.3) as

$$\sigma'_t = \frac{\sqrt{\pi}}{4\rho^3}\operatorname{erf}[\rho] - \exp(-\rho^2)\left(1+\frac{1}{2\rho^2}\right) \tag{5.11}$$

$$\sigma'_r = -\frac{\sqrt{\pi}}{2\rho^3}\operatorname{erf}[\rho] + \frac{1}{\rho^2}\exp(-\rho^2)\ ,\ \rho = r/R \tag{5.12}$$

with the so-called error function erf[ρ]. These stress distributions are shown in Fig. 5.6b.
The stress intensity factor for a circular crack loaded by the tangential stress σ_t can be computed by applying the weight function for the embedded circular crack

$$h = \frac{2}{\sqrt{\pi a}}\frac{r}{\sqrt{a^2-r^2}} \tag{5.13}$$

It results

$$K = \frac{ET\Delta\alpha(0)}{(1-\nu)\sqrt{\pi}}\sqrt{a}\left(\begin{array}{l} -\frac{R}{a}\exp(-(a/R)^2)\operatorname{erf}[a/R] + \\ +\frac{1}{3}\left(3\,HypPFQ[1,1,\tfrac{3}{2},2,-(a/R)^2] - HypPFQ[1,1,2,\tfrac{5}{2},-(a/R)^2]\right)\end{array}\right) \tag{5.14}$$

with the generalised hypergeometric functions HypPFQ. The stress intensity factor is plotted in Fig. 5.7 by the geometric function defined here as

$$F = \frac{1-\nu}{E\Delta T\Delta\alpha(0)\sqrt{a}}\,K \tag{5.15}$$

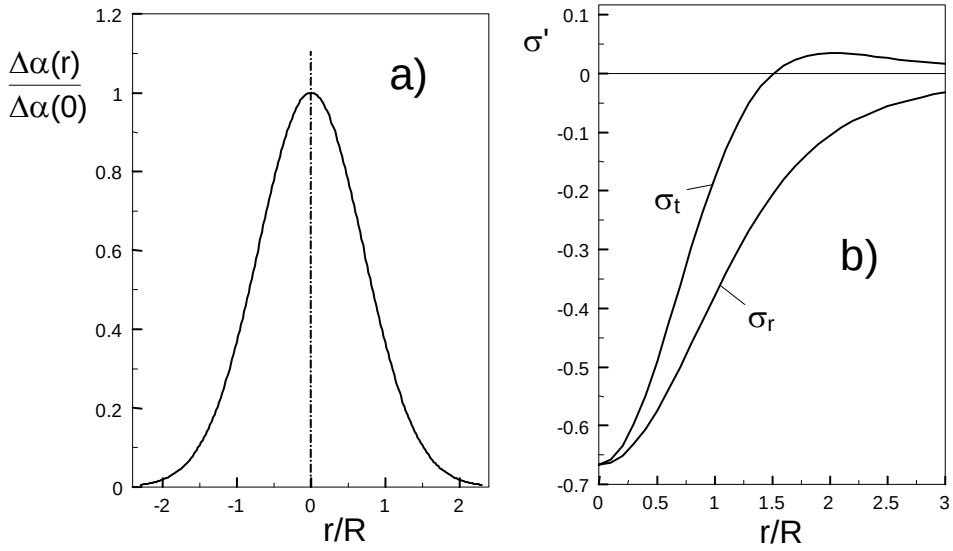

Fig. 5.6 a) Distribution of mismatch of thermal expansion coefficients, b) normalised thermal stresses.

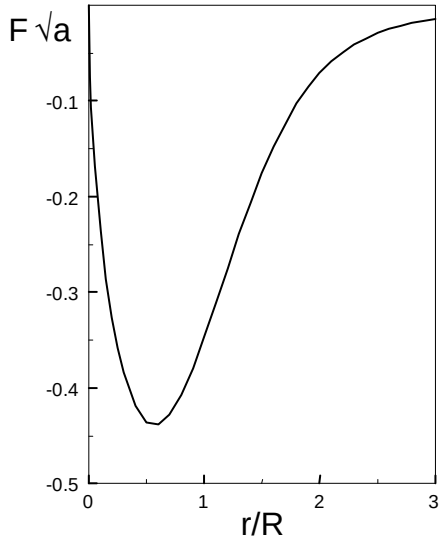

Fig. 5.7 Stress intensity factor for a circular crack.

5.2.2 More general distributions

For a more general distribution of the thermal expansion coefficient in such an inhomogeneity, a simple dependency is

$$\Delta\alpha = \Delta\alpha(0)\exp[-(r/R)^{2n}] \tag{5.16}$$

with integer n. This dependency is plotted in Fig. 5.8 for several values of $2n$. The higher the number n, the steeper is the transition from the inhomogeneity to the matrix. The sphere with a sharp transition is given by the limit $n\to\infty$.

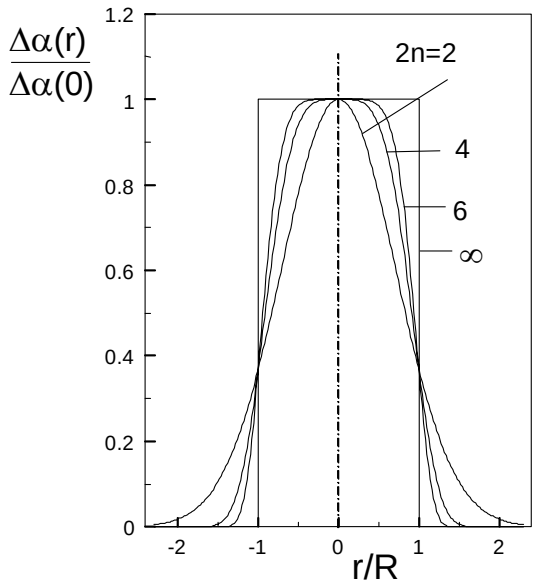

Fig. 5.8 a) Distribution of mismatch of thermal expansion coefficients according to eq.(5.16), b) normalised thermal stresses.

In this case, the stresses are

$$\sigma'_t = \frac{1}{\rho^3}\left(\tfrac{1}{3}\Gamma\left(1+\frac{3}{2n}\right) - \tfrac{1}{2n}\Gamma\left(\frac{3}{2n},\rho^{2n}\right)\right) - \exp(-\rho^{2n}) \tag{5.17}$$

$$\sigma'_r = -\frac{2}{\rho^3}\left(\tfrac{1}{3}\Gamma\left(1+\frac{3}{2n}\right) - \tfrac{1}{2n}\Gamma\left(\frac{3}{2n},\rho^{2n}\right)\right) \tag{5.18}$$

where $\Gamma(x)$ is the complete and $\Gamma(x,y)$ the incomplete gamma function. Figure 5.9 shows the results (5.17) and (5.18) for several n-values. Also from Fig. 5.9a, it can be seen that the maximum tensile stress around the inhomogeneity (tension for $\Delta\alpha\Delta T>0$, compression for $\Delta\alpha\Delta T<0$) decreases with decreasing n, i.e. with a smoother variation of the thermal expansion coefficient α. This becomes obvious from Fig. 5.10, where the maximum tangential tensile stress is plotted versus 1/(2n). The decreasing curve can be approximated by

$$\sigma'_{t,\max} \cong \tfrac{1}{3}[0.536\exp(-3.32/(2n)) + 0.464\exp(-11.31/(2n))] \tag{5.19}$$

The stress intensity factor for a circular crack extending through the inhomogeneity, computed with eq.(5.13), is plotted in the form of $F\sqrt{a}$ in Fig. 5.11.

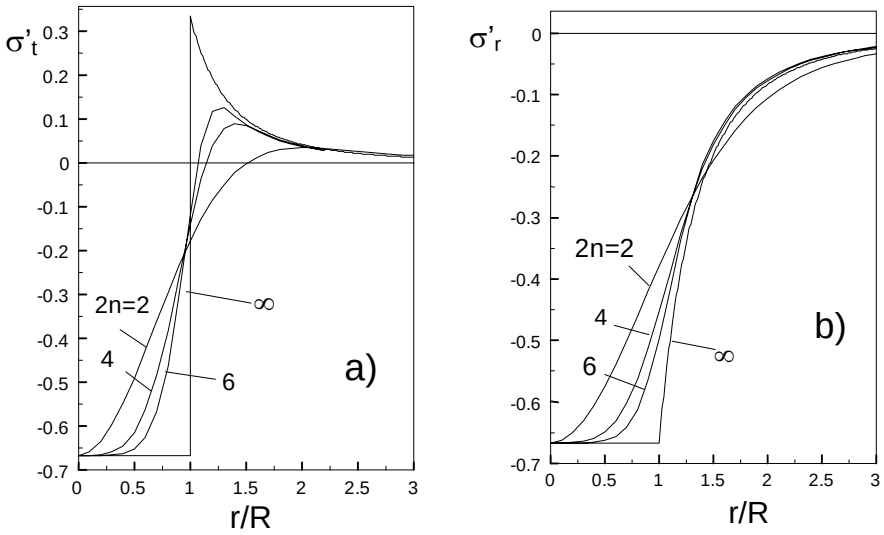

Fig. 5.9 Normalised thermal stresses, a) tangential stress, b) radial stress.

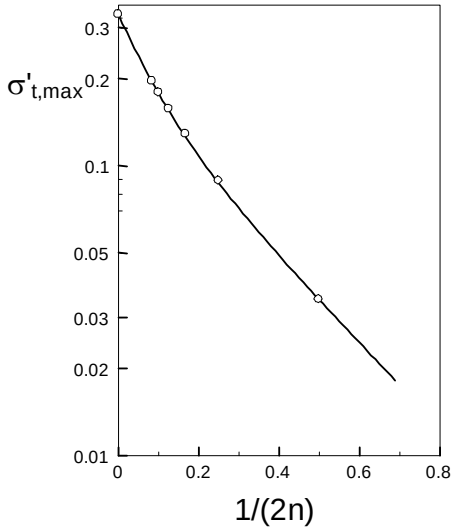

Fig. 5.10 Maximum tangential tensile stress depending on *n*.

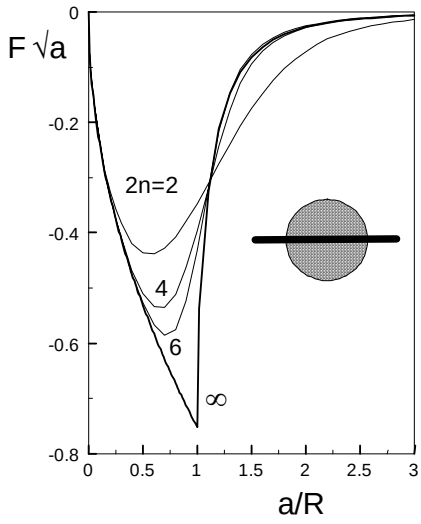

Fig. 5.11 Stress intensity factor for a circular crack extending through the inhomogeneity.

The stress intensity factor for an annular crack with the inner crack tip at $r=R$, computed with the weight function (2.12), is plotted in the form of the geometric function F in Fig. 5.12. From this representation, a decreasing maximum stress intensity factor is visible.

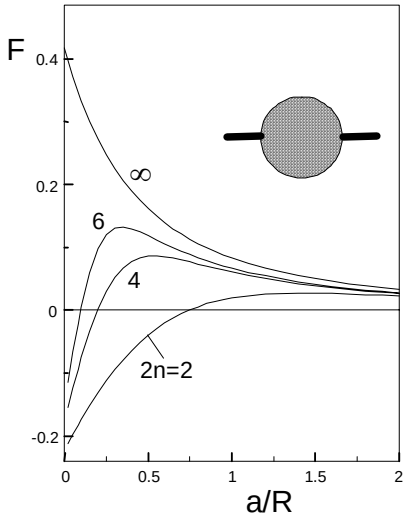

Fig. 5.12 Stress intensity factor for an annular crack with the inner tip located at R.

5.3 Variable Young's modulus

5.3.1 Differential equation for the radial displacements

Modifying the analysis for constant Young's moduli (given in [15], section 132), the problem of a simultaneously changing thermal expansion mismatch $\Delta\alpha$ and elastic constants E and ν can be solved.

Having in mind that for a constant temperature change $\Delta T \neq f(r)$ the elastic strains ε_{el} are given by the local differences of the expansion coefficient, it results from Hooke's law that

$$\varepsilon_{el,r} = \varepsilon_r - \Delta\alpha(r)\,\Delta T = \frac{1}{E(r)}(\sigma_r - 2\nu(r)\sigma_t) \tag{5.20}$$

$$\varepsilon_{el,t} = \varepsilon_t - \Delta\alpha(r)\,\Delta T = \frac{1}{E(r)}[\sigma_t - \nu(r)(\sigma_r - \sigma_t)] \tag{5.21}$$

With the total strains ε_r and ε_t replaced by the radial displacements u according to

$$\varepsilon_r = \frac{du}{dr}\ , \quad \varepsilon_t = \frac{u}{r} \tag{5.22}$$

the stress components yield

$$\sigma_r = \frac{E(r)}{[1+\nu(r)][1-2\nu(r)]}[(1-\nu(r))\varepsilon_r + 2\nu(r)\varepsilon_t - (1+\nu(r))\Delta\alpha(r)\Delta T] \tag{5.23}$$

$$\sigma_t = \frac{E(r)}{[1+\nu(r)][1-2\nu(r)]}[\varepsilon_t + \nu(r)\varepsilon_r - (1+\nu(r))\Delta\alpha(r)\Delta T] \tag{5.24}$$

Inserting these stress components into the radial equilibrium condition

$$\frac{d\sigma_r}{dr} + \frac{2}{r}(\sigma_r - \sigma_t) = 0 \tag{5.25}$$

a somewhat lengthy ordinary differential equation for $u(r)$ results with the highest derivative u''. Therefore, the numerical evaluation was carried out with Mathematica using the option NDSolve.

5.3.2 Determination of stresses for some examples

In the following considerations, the distribution (5.10) is used for the thermal expansion mismatch. Young's modulus is chosen to change in a similar way, namely,

$$E(r) = E_\infty + \Delta E(0)\exp[-(r/R)^2] \ , \quad \Delta E(0) = E_0 - E_\infty \tag{5.26}$$

where E_0 is the value in the centre and E_∞ far away from the inhomogeneity. The variation of ν may be neglected and a fixed value of ν=0.25 is chosen for reasons of simplicity.
From the solution of eq.(5.25), the radial displacements were determined. They are shown in Fig. 5.13 in a normalised form

$$u_{norm} = \frac{u}{R\Delta\alpha(0)\Delta T} \tag{5.27}$$

From the displacements, the strains are computed via eqs.(5.22). Inserting into (5.23) and (5.24) provides the stress components. Here, the tangential stresses are of special interest. They are plotted in Fig. 5.14a in normalised form according to (5.4). The maximum tangential stresses are shown in Fig. 5.14b versus the ratio of the Young's moduli in the centre of the inhomogeneity E_0 and the bulk material E_∞.
The maximum tensile stresses are smaller by a factor of about 10 than those obtained from the model of a sharp transition of material properties from the inclusion to the bulk material.

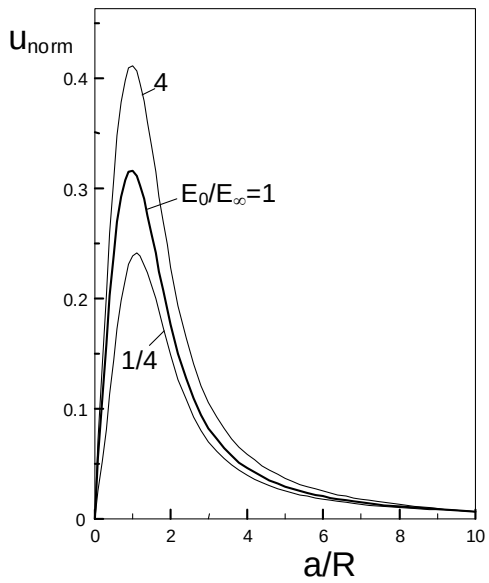

Fig. 5.13 Displacements $u(r)$ in normalised representation (5.27) for different ratios of Young's moduli.

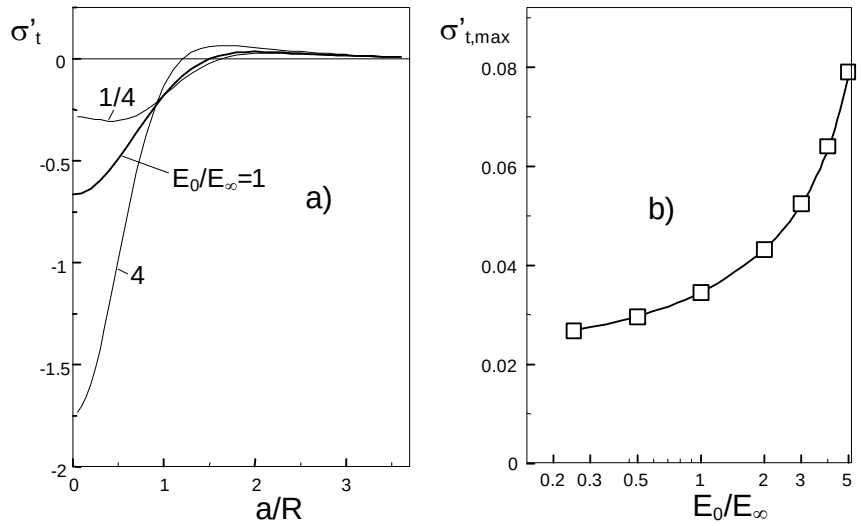

Fig. 5.14 a) Tangential stresses in normalised representation (5.4) for different ratios of Young's moduli, b) maximum tangential stress versus Young's moduli ratio.

In the range of $0.2<E_0/E_\infty\leq 5$, the maximum tangential stresses of Fig. 5.14b can be expressed by

$$\sigma'_{t,\max} \cong 0.024 + 0.01157\frac{E_0}{E_\infty} - 0.001563\left(\frac{E_0}{E_\infty}\right)^2 + 0.00029\left(\frac{E_0}{E_\infty}\right)^3 \qquad (5.28)$$

The maximum tangential stresses are shown again in Fig. 5.15 as a function of the modulus ratio E_0/E_∞. In this plot, the result of Fig. 5.14b is entered as the solid curve. The dash-dotted curve represents the result for a step-shaped variation of the material properties. The square is the maximum tangential stress obtained from eq.(5.19) for 2n=4 and $E_0/E_\infty=1$. Also this comparison clearly shows the stress-reducing effect of a continuous change of material properties. Figure 5.15b shows the influence of the Young's moduli on the stress intensity factor $K_{(A)}$ of an annular crack with the inner tip at $r=R$.

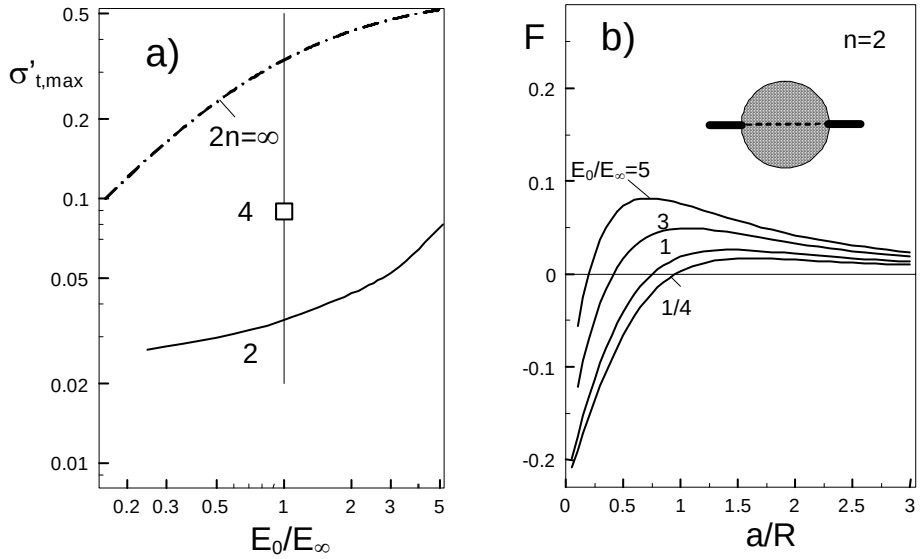

Fig. 5.15 a) Comparison of maximum tangential stresses (solid curve: result from Fig. 5.14b, dash-dotted curve: step-shaped transition of material parameters, square: stress from (5.19) for 2n=4), b) Influence of Young's moduli on the geometric function according to eq.(5.15) for the outer tip of an annular crack..

References

[1] Rosenfelder, O., Fraktografische und bruchmechanische Untersuchungen zur Beschreibung des Versagensverhaltens von Si_3N_4 und SiC bei Raumtemperatur, Dissertation, Universität Karlsruhe, 1986, Karlsruhe, Germany.

[2] Nied, H.F., Erdogan, F., The elasticity problem for a thick-walled cylinder containing a circumferential crack, Int. J. Fract. 22(1983), 277-301.

[3] Tada, H., Paris, P.C., Irwin, G.R., The stress analysis of cracks handbook, Del Research Corporation, 1986.

[4] Fett, T., Munz, D., Stress Intensity Factors and Weight Functions, Computational Mechanics Publications, Southampton 1997.

[5] Baratta, F.I., Mode-I stress intensity factor estimates for various configurations involving single and multiple cracked spherical voids, Fracture Mechanics of Ceramics, Vol. 5, Plenum Press, 1983, 543-567.

[6] Ito, M., Numerical modelling of microcracking in two-phase ceramics, Vol. 5, Plenum Press, 1983, 479-493.

[7] Hill, R., Mathematical Theory of Plasticity, Oxford University Press, 1950, Oxford.

[8] Fett, T., Kounga Njiwa, A.B., Rödel, J., Crack opening displacements of Vickers indentation cracks, Engng. Fract. Mech. **72**(2005), 647-659.

[9] Fett, T., Rizzi, G., Problems in fracture mechanics of indentation cracks, Report FZKA 6907, Forschungszentrum Karlsruhe 2003.

[10] Goodier, J.N., Concentration of stress around spherical and cylindrical inclusions and flaws, J. Appl. Mech. 1933, 39-44.

[11] Baratta, F.I., Stress intensity factor estimates for a peripherally cracked spherical void and a hemispherical surface pit, J. Am. Ceram. Soc. 61(1978), 490-493.

[12] Baratta, F.I., Refinement of stress intensity factor estimates for a peripherally cracked spherical void and a hemispherical surface pit, J. Am. Ceram. Soc. 64(1981), C3-C4.

[13] Green, D.J., Stress intensity factor estimates for annular crack at spherical voids, J. Am. Ceram. Soc. 63(1980), 342-344.

[14] Green, D.J., Stress-induced microcracking of second-phase inclusions, J. Am. Ceram. Soc. 64(1981), 138-141.

[15] Timoshenko, S.P., Goodier, J.N., Theory of Elasticity, McGraw-Hill Kogagusha, Ltd., 1970, Tokyo.

[16] Dhaliwal, R.S., Rokne, J.G., Singh, B.M., Penny-shaped crack in a sphere embedded in an infinite medium, Int. J. Engng. Sci. 17(1979), 259-269.

[17] Karihaloo, B.L., Huang, X., Asymptotics of three-dimensional macrocrack-microcrack interaction, Int. J. Solids Struct. 32(1995), 1495-1500.

APPENDIX

A1. Central penny-shaped crack in a spherical inclusion

In the preceding sections, the interaction of stress fields around inclusions with an annular crack was addressed. Another case of interest is the crack in the inclusion. This problem shall now be addressed briefly.

Figure A1 shows the crack of radius a in a sphere of radius *R*. The stress intensity factor solution under thermal stresses and remote tension was approximated by Rosenfelder [1] applying the weight function for a homogeneous material. This results in

$$K_I = \frac{2}{\sqrt{\pi a}} \int_0^a \frac{\sigma(r) r}{\sqrt{a^2 - r^2}} dr \tag{A1}$$

Equation (A1) is exact for the limit case $a/R \to 0$. For crack sizes comparable with the inclusion radius, deviations have to be expected. Equation (A1) must become incorrect for $a/R=1$, since the stress singularity at a crack tip is different from the $\sqrt{r}$ singularity of K_I in this case. For an assessment of the accuracy of (A1), the case of a constant pressure on the crack faces may be considered. Inserting $\sigma(r)=\sigma_0$ in (A1) gives the well-known result for a circular crack in an infinite body

$$K_\infty = \frac{2}{\sqrt{\pi}} \sqrt{a}\, \sigma_0 \tag{A2}$$

A numerical analysis of the case of constant loading was performed by Dhaliwal et al. [16] for the special case of identical Poisson ratios $\nu_1=\nu_2=1/3$. The stress intensity factor normalised to the value K_∞ is plotted in Fig. A2 for several ratios of shear moduli $\Gamma=\mu_2/\mu_1$ (μ_1= shear modulus of the inclusion, μ_2= shear modulus of the matrix). The horizontal straight line, $K_I/K_\infty=1$, corresponds to the result of the approximation (A1).

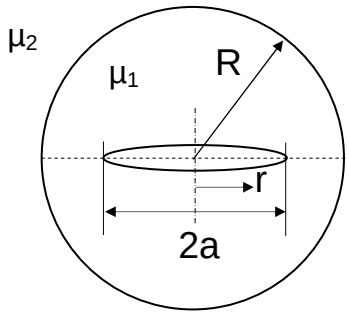

Fig. A1 Spherical inclusion containing a central penny-shaped crack.

From Fig. A2, it is concluded that for material combinations in the range of $0.5 \le \Gamma \le 3$, the error of (A1) is less than 10% for $a/R<0.65$. Therefore, it is recommended to restrict the

application of eq.(A1) to $a/R<0.65$ for the evaluation of more complicated stress distributions (e.g. thermal stresses).

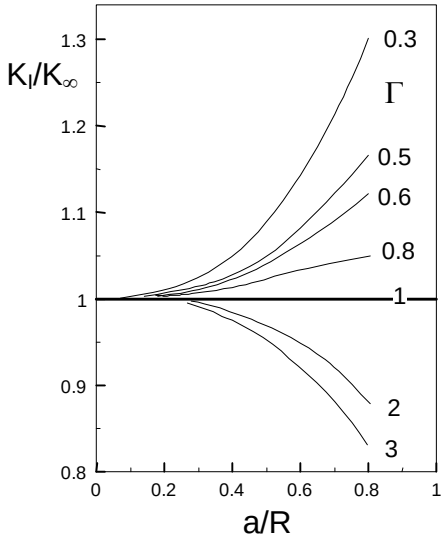

Fig. A2 Stress intensity factor of a circular crack in an inclusion under constant crack-face loading normalised to the stress intensity factor of a circular crack in a half-space [16].

For cracks with $a>R$, Rosenfelder [1] proposed the application of the same weight function as used in eq.(A1). Stress intensity factor solutions for thermal stresses and remote tractions are reported in [1].

A2. Circular crack

A2.1 Remote and cylinder-symmetric stresses

A circular crack is the limit case $a/R\to\infty$ for the pore as well as for the inclusion with an annular crack. The stress intensity factor under rotationally symmetric stress distributions can be computed from eq.(A1). For a constant remote stress σ_0, the stress intensity factor is given by eq.(A2).

A2.2 Circular crack under non-symmetric stress

A2.2.1 Stress intensity factors for a circular crack ahead of the main crack

If the circular crack of radius a at distance d from the tip of the main crack (Fig. A3a) is loaded by an applied stress σ_{appl} that varies over the diameter,

$$\sigma_{appl}(r)=\frac{K_{appl}}{\sqrt{2\pi r}}\Rightarrow\sigma_{appl}(x)=\frac{K_{appl}}{\sqrt{2\pi(x+d+a)}} \tag{A3}$$

where K_{appl} is the actual stress intensity factor for the main crack. The stress intensity factors at locations (A) and (B) can be computed from

$$K_A=\frac{1}{\sqrt{\pi a}}\left[\sqrt{2a}\int_{-a}^{a}\frac{\sigma(x)}{\sqrt{x+a}}dx-\int_{-a}^{a}\sigma(x)dx\right] \tag{A4}$$

$$K_B = \frac{1}{\sqrt{\pi a}}\left[\sqrt{2a}\int_{-a}^{a}\frac{\sigma(x)}{\sqrt{a-x}}dx - \int_{-a}^{a}\sigma(x)dx\right] \tag{A5}$$

as given by Tada ([3], page 24.12). Under loading by a crack-tip stress field, the stress intensity factor at point (A) is larger than at point (B).
Inserting (A3) into (A4) yields

$$K_A = \frac{K_{appl}\sqrt{2}}{\pi}\left[\sqrt{\frac{d}{a}} - \sqrt{2+\frac{d}{a}} + \frac{1}{\sqrt{2}}\ln\left(1+4\frac{a}{d}+\sqrt{8a/d}\sqrt{1+\frac{2a}{d}}\right)\right] \tag{A6}$$

$$K_B = \frac{K_{appl}\sqrt{2}}{\pi}\left[\sqrt{\frac{d}{a}} - \sqrt{2+\frac{d}{a}} + \frac{1}{\sqrt{2}}\left(\frac{\pi}{2} - \arctan\frac{1-2a/d}{\sqrt{8a/d}}\right)\right] \tag{A7}$$

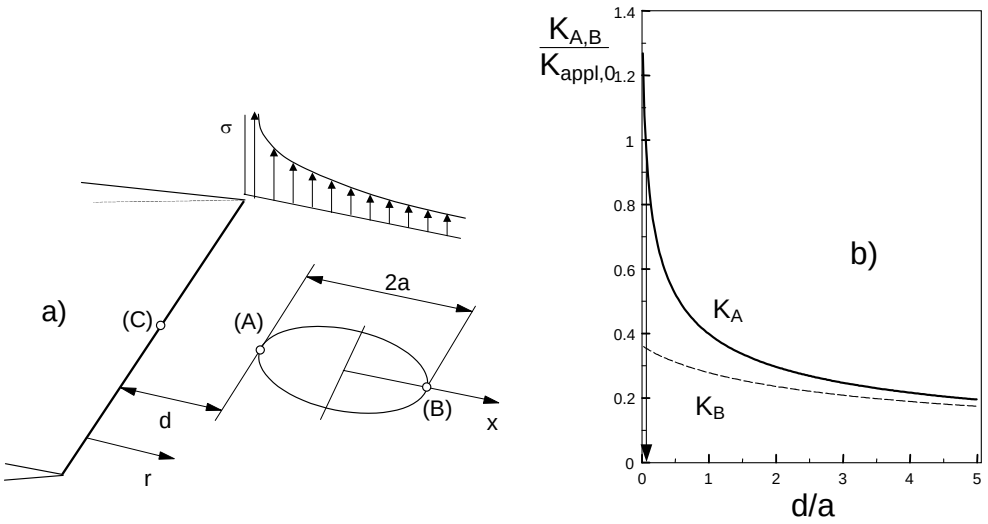

Fig. A3 a) Circular microcrack ahead of the main crack tip, b) stress intensity factors for locations (A) and (B), vertical arrow indicates the ratio d/a=0.066, for which K_A/K_{appl}=1 is fulfilled.

The stress intensity factors are plotted in Fig. A3b versus the normalised distance d/a. For cracks at larger distance ($d>>a$), it follows simply

$$K_A = K_B = \frac{\sqrt{2}}{\pi}\sqrt{\frac{a}{d}}K_{appl} \tag{A8}$$

A2.2.2 Effect of a circular crack ahead of the main crack on the applied stress intensity factor

A microcrack in front of the main crack may also influence the stress intensity factor of the main crack. This situation was studied by Karihaloo and Huang [17]. The stress intensity factor K_C at the nearest distance (point C in Fig. A3a) is plotted in Fig. A4a as a function of the normalised distance d/a of the microcrack. The data of Fig. A4a can be fitted by

$$K_C = K_{appl,0}\left(1+0.056\left(\frac{a}{d}\right)^{2/3}\right) \tag{A9}$$

where $K_{appl,0}$ is the applied stress intensity factor, if no microcrack exists in front of the main crack. From the diagram Fig. A4a, it can be concluded that the main crack stress intensity factor is only changed for more than 10%, if $d/a<0.2$.

The normalised stress intensity factors $K_A/K_{appl,0}$ and $K_B/K_{appl,0}$ are plotted in Fig. A4b. The upper limit curve is computed under the assumption that the circular crack is influenced by the stress intensity factor K_C. The lower limit curve is computed assuming the externally applied stress intensity factor $K_{appl,0}$ as the loading parameter. In reality, the true solution must be between the two limit cases. The stress intensity factor K_C is the maximum value along the front of the main crack. At larger distance, the K-value tends to $K_{appl,0}$. In order to minimise the uncertainty, we propose for the true applied stress intensity factor K_{appl}

$$K_{appl} \cong K_{appl,0}\left(1+0.03\left(\frac{a}{d}\right)^{2/3}\right) \tag{A10}$$

This value has to be inserted into eqs.(A6) and (A7).

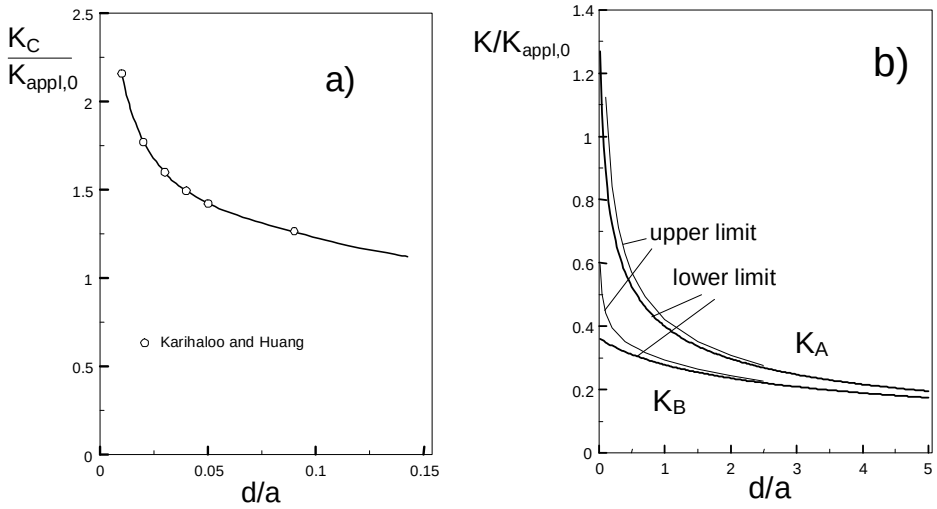

Fig. A4 a) Influence of a microcrack on the stress intensity factor K_C at the front of the main crack, b)upper and lower limits for the stress intensity factors at the circular crack.